

Grid Quality and Resolution Effects on the Aerodynamic Modeling of Ram-Air Parachute Canopies

Mehdi Ghoreyshi^{1*}, Keith Bergeron^{2†}, Jürgen Seidel^{1‡}
Andrew J. Lofthouse^{1§}, Russell M. Cummings^{1¶}

¹ *High Performance Computing Research Center, U.S. Air Force Academy
USAF Academy, Colorado 80840*

² *US Army Natick Research, Development, and Engineering Center
Natick, MA 01760*

This work provides an overview of the grid quality and resolution effects on the aerodynamic modeling of ram-air parachute canopies. The CFD simulations were performed using the Cobalt flow solver on two dimensional canopy sections with open and closed inlets. Previous simulation results of these geometries showed that grid independence is achieved for the closed and open airfoils with grids containing around half a million and two million cells, respectively. Previous grids were either hybrid with prismatic layers near the walls or multi-block structured using algebraic grid generators. The results presented in this work show that grid independence of both geometries can be achieved with much coarser grids. These grids, however, were generated with good smoothness, wall orthogonality, and skewness qualities. The results show that the grid quality value is mainly related to the grid smoothness and does not depend on the mesh skewness or the wall orthogonality. Although a smooth grid improves the quality value and therefore the solution convergence, it does not always lead to an accurate solution. For example, the unstructured meshes with anisotropic cells near the wall have very good grid quality, however they have the worst accuracy among all meshes considered because of the poor skewness at the walls. The results also showed that in comparison to the closed inlets, the open geometry solutions are less sensitive to the initial grid spacing and number of constant spacing layers at the outside airfoil walls. Finally, the open inlet solutions do not change with the inside airfoil mesh resolution and type.

Nomenclature

a	speed of sound, m/s
C_L	lift coefficient, $L/q_\infty S$
C_D	drag coefficient, $D/q_\infty S$

*Senior Aerospace Engineer, AIAA Senior Member

†Senior Research Aerospace Engineer, AIAA Senior Member

‡Senior Aerospace Engineer, AIAA Senior Member

§Director, AIAA Senior Member

¶Professor of Aeronautics, AIAA Associate Fellow

Distribution A. Approved for Public Release. Distribution unlimited.

C_p	pressure coefficient, $(p - p_\infty)/q_\infty$
c	mean aerodynamic chord, m
D	drag force, N
GQ	grid quality
GR	growth rate in the viscous layer
L	lift force, N
l	farfield distance away from the airfoil, m
M	Mach number, V/a
N_s	the number of layers of constant spacing normal to all viscous walls
p	static pressure, Pa
p_∞	freestream pressure, Pa
q_∞	dynamic pressure, Pa, $\rho V^2/2$
q_k^i	k^{th} grid quality metric at i^{th} cell
Re	Reynolds number, $\rho V c/\mu$
S	Planform area, m^3
t	time, s
V	freestream velocity, m/s
x, y, z	grid coordinates
y^+	non-dimensional wall distance

Greek

Δ_{s1}	the initial spacing at all viscous walls
η, ζ, ξ	mesh orientation vector
α	angle of attack, deg
ρ	air density, kg/m^3
μ	air viscosity, $\text{kg}/(\text{m}\cdot\text{s})$

I. Introduction

The accuracy and expediency of computational fluid dynamic (CFD) solutions depend not only on the underlying numerical methods, but also on the grid generation process in which the computational domain is discretized into distinct sub-domains. These sub-domains are called cells or grid blocks. The numerical error rises if the physical geometry is not exactly represented by the grid.¹ Also, truncation error and machine round-off error are always present in the numerical solutions of partial or ordinary differential equations.² These errors depend on the grid size such that for a finer mesh, the truncation errors decreases, but the rounding errors will increase. Finally, inaccurate interpolation of the discrete solutions between grid blocks will increase the numerical error.

Uniform grids have many advantages over non-uniform grids including a better accuracy and faster convergence.³ However, to resolve boundary layer and wake regions in viscous flows, a uniform grid approach would require a very large number of mesh points, which increases the computational cost. Practical turnaround times for obtaining a CFD solution and availability of computer facilities would limit the uniform grid applicability for three-dimensional (3D) problems. The total number of mesh points, and therefore computational cost, can be reduced by using a non-uniform grid approach, in which the grid points are clustered near the regions of interest and are coarsely distributed elsewhere. However, these non-uniform cells can sometimes lead to grids of locally poor quality that will increase the computational solution error.⁴ The performance of numerical methods can be significantly reduced even if just a few low-quality cells are present.⁵

Grid generation efforts can be traced back to the 1960s. Since then many grid generation methods have been proposed such as conformal mapping, algebraic construction, partial differential equation solutions (elliptic, hyperbolic, and parabolic equations), Delaunay, advancing-front, and many others.¹ These methods have been used to generate structured and/or unstructured meshes over simple to complex geometries. Each method leads to a different grid quality for a given geometry. Besides, while some mesh generation methods could be fast and even automated, others are a time consuming manual process.

Conformal mapping is the simplest method of structured grid generation, in which the computational domain is mapped onto a rectangular region. Although the method is simple and efficient and creates very high quality cells, it is practical only for simple two-dimensional problems. To create a smooth structured grid, elliptic grid generators can be used, which involve the numerical solution of inhomogeneous elliptic partial differential equations.⁶ Grid smoothness can help reduce the truncation error and improve the accuracy. A disadvantage of the elliptic grid generation is the limited control over the interior grid points. Algebraic methods have also been used to create structured meshes. These methods use algebraic transformation and an interpolation scheme to distribute grid points from a discrete set of data.⁷ In comparison to elliptic grid generators, algebraic methods require much less computational effort and have better control over grid point locations, but the grid may not be as smooth as an elliptic grid. To improve the interior mesh over complex geometries, the multi-block strategy has been proposed, in which the computational domain is divided into several smaller sub-domains (block) and then separate meshes are generated for each block.⁸ Each block can initially be meshed by an algebraic method and then an elliptic solver is used to smooth the meshes.

Although structured meshes offer higher accuracy, simplicity, and easy data access compared to an unstructured mesh, unstructured meshes (using tetrahedra cells) are more popular for complicated geometries.⁹ Delaunay and advancing-front methods are the most popular tetrahedral mesh generators. The advancing front creates the cells one by one, starting from the domain boundary and by marching a *front* toward the interior.¹⁰ The *front* refers to the cells that meet unmeshed domains; the front will eventually vanish when the mesh is completed. Advancing-front approach will have the best quality cells at the boundaries and the worst cells where the front collides with itself.¹⁰ Therefore, this mesh generator is very helpful for modeling inviscid or laminar flows over solid walls. The advancing-front method can even be used to create quadrilateral cells, however, the interior cells could have low quality or the mesh may not be completed for a complex geometry. Typical Delaunay mesh generators start from a boundary discretization. New points and triangular cells are then added to satisfy a particular connectivity. The method maximizes the minimum angle of all triangles to avoid sharp and distorted cells wherever possible.¹¹ Delaunay mesh generators, unlike advancing-front method, have the worst cells at the domain boundary and the best cells in the interior.¹⁰ Therefore, the Delaunay and the advancing front approaches are often combined to use the advantages of both methods.

Unstructured meshes are not effective when localized regions of high gradients appear in the flow, such as boundary layers.¹² Hybrid grid generators and anisotropic tetrahedral extrusion are commonly used to treat boundary layers in unstructured meshes. The first step of a hybrid approach is the triangulation of the computational domain and then placing prismatic cells near boundary surfaces. The prismatic cells are typically created using an advancing layer scheme. In such a mesh, the outside boundary nearly has isotropic tetrahedral cells.¹³ A disadvantage is that prismatic cells may have poor quality near sharp edges. An anisotropic tetrahedral extrusion creates triangular cells in a layer-by-layer fashion with the extrusion direction normal to the surface.¹² The method begins with an isotropic tetrahedral mesh (generated by Delaunay and/or advancing-front methods), and tetrahedra on surfaces are then subdivided into anisotropic cells for user-specified number of layers.¹⁴ However, this approach might create extremely stretched tetrahedra cells near the walls which impact the accuracy of computations.

At the United States Air Force Academy (USAFA), the hybrid mesh approach has been successfully used for a number of years for CFD simulation of many fighter aircraft.^{15, 16, 17, 18} These grids have structured cells near solid surfaces and unstructured cells elsewhere. Specifically, an inviscid tetrahedral mesh is generated using the ICEM-CFD code. This mesh will then be used as a background mesh by the mesh generator TRITET^{19, 20} which builds prism layers using a frontal technique. TRITET rebuilds the inviscid mesh while respecting the size of the original inviscid mesh from ICEM-CFD. More recently, the authors of this work used this hybrid grid approach for prediction of aerodynamic characteristics of a ram-air parachute.^{21, 22} The grid sensitivity study showed that solutions are very sensitive to the grid quality and size for the airfoils/wings with an open inlet. For example the airfoil solutions became grid independent for the hybrid grids that have more than 1.7 million cells. That brings to mind a question whether another grid generator could produce similar predictions to the hybrid fine grids, but at a much lower computational cost.

The objectives of the work presented here are twofold: one concerns the grid resolution and to find coarse grids that can have comparable results to the fine meshes. Second, is to understand the relationship between mesh quality and the solution accuracy and convergence. Results are presented for two-dimensional airfoils with open and closed inlet. These results can be easily generalized to three-dimensional wings. For example, a high quality 3D mesh can be created from spanwise extrusion of a high quality 2D mesh. This work is

organized as follows. First the Cobalt flow solver is described. Several grid quality metrics are also reviewed. Next, the test case is presented. Finally, the simulation results will be discussed.

II. CFD Solver

This study uses the commercial flow solver Cobalt which solves the unsteady, three-dimensional, compressible Navier-Stokes equations in an inertial reference frame. Arbitrary cell types in two or three dimensions may be used; a single grid therefore can be composed of different cell types.²³ In Cobalt, the Navier-Stokes equations are discretized on arbitrary grid topologies using a cell-centered finite volume method. Second-order accuracy in space is achieved using the exact Riemann solver of Gottlieb and Groth,²⁴ and least squares gradient calculations using QR factorization. To accelerate the solution of the discretized system, a point-implicit method using analytic first-order inviscid and viscous Jacobians is used. A Newtonian sub-iteration method is used to improve the time accuracy of the point-implicit method. Tomaro et al.²⁵ converted the code from explicit to implicit, enabling Courant-Friedrichs-Lewy (CFL) numbers as high as 10^6 . In Cobalt, the computational grid can be divided into group of cells, or zones, for parallel processing, where high performance and scalability can be achieved even on thousands of processors.²⁶ Some available turbulence models in Cobalt are the Spalart-Allmaras (SA) model,²⁷ Spalart-Allmaras with Rotation Correction (SARC),²⁸ and Delayed Detached-eddy simulation (DDES) with SARC.²⁹

Cobalt checks the grid quality and reports a score; this score is directly related to a particular part of the second-order accurate spatial operator inside Cobalt.³⁰ The reported score is averaged over all the cells and ranges from zero to hundred, such that the lower the grid score, the more numerical dissipation is added to the solution (worse stability). Note that Cobalt's grid score involves the mesh geometry information only, and not the flow solution obtained on that mesh. This means that the grid quality is a fixed number regardless of the angle of attack and Mach number. Cobalt's User Guide³⁰ details that the high aspect ratio of cells (typically placed in the boundary layer) can cause the quality to suffer. Also, regions of high surface curvature can adversely impact grid quality. The grid quality will improve if a sufficient number of surface cells are used to accurately capture any geometric curvature.

III. Grid Quality Measures

The relationship between the mesh quality and solution accuracy will be investigated in this work. A priori grid quality metrics could provide some guidance of the grid before running it in CFD.³¹ The mesh quality mainly deals with the geometric information of the grid. Before examining the grid quality, one should check the grid for negative volume (or volumes below a threshold) and folded cells. These type of cells make a cell-centered flow solver impossible to iterate.³² Typically, a high quality mesh is obtained by creating well-shaped cells (orthogonal structured cells or isotropic tetrahedra cells) with moderate smoothness. Therefore, most grid quality metrics indicate how much a grid cell deviates from its ideal shape.

A great, but more advanced, way to improve the grid quality metrics is to add information about the numerical solution obtained on the mesh.⁴ One simple example is y^+ values at the walls. According to the gridding guidelines from the 2nd AIAA CFD high lift prediction workshop,³³ approximate initial spacing normal to all viscous walls should have y^+ values of approximately 1.0, 2/3, 4/9, and 8/27 for a coarse, medium, fine, and extra fine grid, respectively. In more advanced grid generation methods, the solution errors are used to refine the mesh in regions where the error is large.

Mesh resolution and quality should be checked prior to running the grid in CFD. The mesh resolution should be high enough to capture the flow physics. Mavriplis et al.,³⁴ for example, have recommended a chordwise grid spacing of 0.1% of local chord (for a medium grid) at the wing leading and trailing edges. In the spanwise direction at the wing root and tip, a grid spacing of 0.1% of semispan was recommended. The grid dimension (size) at the wing trailing edge base is recommended to be 8, 12, 16, 24 for a coarse, medium, fine, and extra fine grid, respectively. The grid resolution can be evaluated by sensitivity studies. The results become mesh independent if they show less than 3% difference from a 30% finer mesh.³⁵

The grid quality is often measured for each cell from given information about the cell's aspect ratio and skewness. It is also desirable to have near-wall faces parallel to the wall. Besides, the rate at which the grid spacing changes from one cell to another (grid smoothness) is important. Optimal grids have equilateral cells (equilateral triangles and squares) with a smooth change of dimensions through the domain.³⁵ In more details, cell skewness should be kept minimum. High aspect ratios would slow down the convergence. Finally,

a spacing growth rate below 20% does not affect the solutions,³⁵ but higher values affect the solution accuracy and convergence. The reader should note that these criteria might change from one solver to another. This is discussed later in this section.

There are some available grid quality metrics. Alter,³⁶ for example, has described a grid quality metric for structured three-dimensional grids. This metrics is defined by,

$$\text{GQ} = \frac{\bar{\theta}_{\min} \bar{\Theta}}{\bar{\epsilon}_{\max}} \quad (1)$$

where GQ denotes the grid quality ranging from zero to one; $\bar{\theta}_{\min}$, $\bar{\Theta}$, and $\bar{\epsilon}_{\max}$ show deviations from orthogonality, straightness, and stretching, respectively. Best grid quality comes with $\text{GQ} = 1$. The minimum of the average skewness, $\bar{\theta}_{\min}$, is determined in three directions by

$$\theta |_{\xi=\text{constant}} = \frac{2}{\pi} \cos^{-1} \left(\frac{\vec{r}_{\eta} \cdot \vec{r}_{\zeta}}{|\vec{r}_{\eta}| |\vec{r}_{\zeta}|} \right) \quad (2)$$

$$\theta |_{\eta=\text{constant}} = \frac{2}{\pi} \cos^{-1} \left(\frac{\vec{r}_{\xi} \cdot \vec{r}_{\zeta}}{|\vec{r}_{\xi}| |\vec{r}_{\zeta}|} \right) \quad (3)$$

$$\theta |_{\zeta=\text{constant}} = \frac{2}{\pi} \cos^{-1} \left(\frac{\vec{r}_{\xi} \cdot \vec{r}_{\eta}}{|\vec{r}_{\xi}| |\vec{r}_{\eta}|} \right) \quad (4)$$

which is zero and minimum for a collapsed cell and is one and maximum for an orthogonal edge segment. The straightness, $\bar{\Theta}$, measures the extra distance traversed between the wall and the outer boundary and is computed normal to the boundary as

$$\bar{\Theta} = \frac{S |_{(\zeta_{\min} \rightarrow \zeta_{\max})}}{\sum_{\zeta=1}^{\zeta_{\max}} |\vec{r}|_{\zeta}} \quad (5)$$

where the grid line straightness ranges from zero to one, where zero is for a grid line that begins and ends at the same point. Finally, the maximum average planar stretching, $\bar{\epsilon}_{\max}$, measures the spacing of one point to the next in all three directions and is given by

$$\epsilon_{\xi} = \frac{\max(|\vec{r}_{\xi}^{+}|, |\vec{r}_{\xi}^{-}|)}{\min(|\vec{r}_{\xi}^{+}|, |\vec{r}_{\xi}^{-}|)} \quad (6)$$

$$\epsilon_{\eta} = \frac{\max(|\vec{r}_{\eta}^{+}|, |\vec{r}_{\eta}^{-}|)}{\min(|\vec{r}_{\eta}^{+}|, |\vec{r}_{\eta}^{-}|)} \quad (7)$$

$$\epsilon_{\zeta} = \frac{\max(|\vec{r}_{\zeta}^{+}|, |\vec{r}_{\zeta}^{-}|)}{\min(|\vec{r}_{\zeta}^{+}|, |\vec{r}_{\zeta}^{-}|)} \quad (8)$$

where each term ranges from one as minimum to infinity. The minimum refers to a uniform spacing. An abrupt change in the spacing increases the stretching value. Some examples of orthogonality, stretching, and straightness are shown in Figure 1. For quadrilateral (two-dimensional) meshes, Dannenhoffer³¹ defined the quality metrics of:

$$\text{skew} = \frac{\min(d_1, d_2)}{\max(d_1, d_2)} \quad (9)$$

$$\text{taper} = \min\left(\frac{s_1}{s_3}, \frac{s_3}{s_1}, \frac{s_2}{s_4}, \frac{s_4}{s_2}\right) \quad (10)$$

$$\text{aspect ratio} = \frac{\min(s_1 + s_3, s_2 + s_4)}{\max(s_1 + s_3, s_2 + s_4)} \quad (11)$$

$$\text{stretch} = \sqrt{\frac{\min(A_1, A_2, A_3, A_4)}{\max(A_1, A_2, A_3, A_4)}} \quad (12)$$

where $s_1, s_2, s_3,$ and s_4 are the lengths of the adjacent sides around the cell; d_1 and d_2 are the lengths of two diagonals, and A_1, A_2, A_3 and A_4 are the areas of four cells that surround a node. All these metrics are computed at each cell and then are added to find the overall grid quality.

A grid quality metric based on the deviation from an ideal cell shape will probably invalidate most of anisotropic cells near the walls for viscous flows. On the other hand, these anisotropic cells are allowed in many flow solvers. In addition, for all cell-centered flow solvers, the quadrilateral faces should be planar, however, non-planar faces are not an issue in most node-based solvers. McDaniel³² therefore proposed that an independent mesh quality should be provided from the viewpoint of each flow solver (cell-centered, node-based and others). He then introduced grid quality metrics for the kCFD³⁷ which solves the unsteady, three-dimensional, compressible RANS equations on hybrid unstructured grids. Note that both Cobalt and kCFD code originated from the Air Vehicles Unstructured Solver (AVUS, formally known as Cobalt60²⁴), which is a parallel, implicit, unstructured flow solver developed by the Air Force Research Laboratory. Both solvers have since been highly modified. McDaniel then defined some grid quality metrics which are applicable to most cell-centered numerical algorithms and all cell types and take into account the fact that large-area faces have a larger flux contribution to the solution value in the cell. All metrics lie in the range from zero to one, where one represents the maximum quality. Some of these quality metrics are briefly reviewed in this paper.

Assume that there are no folded and negative volume cells. A planariness metric is defined for the j^{th} face of the i^{th} cell as

$$q^i_{\text{planar},j} = \begin{cases} 1 & \text{face nodes} \leq 3 \\ \left[1 - \frac{\cos^{-1}(\hat{n}_{j,1} \cdot \hat{n}_{j,2})}{\pi}\right] & \text{face nodes} = 4 \end{cases} \quad (13)$$

where $\hat{n}_{j,1}$ and $\hat{n}_{j,2}$ are the unit-normal vectors to each face. The cell planariness metric is then calculated as:

$$q^i_{\text{planar}} = \frac{1}{\sum_j A_j^i} \sum_{j=1}^{\text{No. faces}} A_j^i q^i_{\text{planar},j} \quad (14)$$

A_j^i denotes j^{th} face area of the i^{th} cell. Figure 2 (a) gives the planariness metric values for some example cells. The skew-smoothness metric for the j^{th} face in the i^{th} cell is also defined as

$$q^i_{\text{skew-smooth},j} = \left[\frac{\min(|\bar{\nu}_{\text{left},j}|, |\bar{\nu}_{\text{right},j}|)}{\max(|\bar{\nu}_{\text{left},j}|, |\bar{\nu}_{\text{right},j}|)} \right] \left[\frac{1}{2} (1 - [\hat{\nu}_{\text{left},j} \cdot \hat{\nu}_{\text{right},j}]) \right] \quad (15)$$

$\bar{v}_{\text{left},j}$ and $\bar{v}_{\text{right},j}$ are the vectors from the adjoining left and right cell centroids, respectively, to the centroid of the j^{th} face of the cell. $\hat{v}_{\text{left},j}$ and $\hat{v}_{\text{right},j}$ are the corresponding unit vectors. The first and second terms of equation 15 correspond to the degree of smoothness and skewness across a particular face, respectively. The cell skew-smoothness metric can be calculated using Eq. 14. If the cell is folded then $q^i_{\text{skew-smooth},j} = 0$. The skew-smoothness metric values for some example cells are given in Figure 2 (b).

A flow alignment (wall orthogonality or straightness) metric was also defined to measure the degree to which cell faces are parallel to the solid walls. The flow alignment metric for the j^{th} face in the i^{th} cell is

$$\tilde{q}^i_{\text{align},j} = \frac{\cos^{-1} \left(\text{abs} \left(\hat{n}_{\text{wall}} \cdot \hat{n}^i_{\text{face},j} \right) \right)}{\pi/2} \quad (16)$$

$$q^i_{\text{align},j} = 2 \left[\max \left(\tilde{q}^i_{\text{align},j}, 1 - \tilde{q}^i_{\text{align},j} \right) - 0.5 \right] \quad (17)$$

\hat{n}_{wall} is the unit normal of the closest solid wall boundary face and $\hat{n}^i_{\text{face},j}$ is the unit normal of the j^{th} face. Some flow alignment metric examples are shown in Figure 2 (c). Other quality metrics include isotropy and spacing metrics which measure the deviation from an ‘‘equilateral’’ cell shape and uniformity in the mesh, respectively. The global grid quality is then estimated by

$$\text{GQ} = \sum_{k=1}^{\text{No of metrics}} P_k \left[\sum_{i=1}^{\text{No of cells}} w \left(\bar{s}_k, \hat{d}_{\text{wall},i} \right) q_k^i \right] \quad (18)$$

where P_k is the global weight for the k^{th} quality metric; q_k^i is the k^{th} quality metric value for the i^{th} cell; $w \left(\bar{s}_k, \hat{d}_{\text{wall},i} \right)$ is a weighting function for each quality metric which depends on through parameter \bar{s}_k and $\hat{d}_{\text{wall},i}$, the minimum distance of the i^{th} cell centroid from the solid wall boundary, normalized by the characteristic length for the mesh.

IV. Test Cases/Previous Results

The U.S. Department of Defense (DoD) program to develop precision guided airdrop systems is known as the Joint Precision Airdrop System (JPADS) which is coordinated by the U.S. Army Natick Soldier Center (NSC). The JPADS uses round and ram-air parachutes (parafoils) for deceleration and control of the payload.³⁸ Different type of airfoil sections have been used for parafoils: initial ram-air canopies used the Clark-Y section which has good lift-to-drag (L/D) characteristics for medium Reynolds numbers, Re .³⁹ Over the years this airfoil shape has been modified for parachute applications to improve lift-to-drag ratio; recent canopy designs are based on the airfoil sections used in glider design (for example NASA LS1-0417 airfoil).⁴⁰ In this work, the low-speed airfoil section of an actual parafoil is investigated. The airfoil considered here is a non-symmetric airfoil that has a flat bottom surface. The flow around this airfoil has been studied by Ghoreyshi et al.^{21,22} for open and closed inlets; the open and closed-inlet geometries are shown in Figure 3.

Ghoreyshi et al.²¹ performed the mesh-independence study of both airfoils. These results are shown in Figures 4 and 5. Closed airfoil grids are fully structured or hybrid; structured grids were generated using the multi-block techniques inside the commercial code of Pointwise V17.01.R3. Hybrid meshes were generated using ICEM-CFD and the mesh generator TRITET. All the meshes labeled in Figure 5 are of hybrid type.

Figure 4 shows that the solutions of structured medium (around 663,000 cells) and fine meshes (around 3 million cells) match everywhere. The solutions of the hybrid medium mesh (around 744,000 cells) are in close agreement with the medium and fine structured meshes as well. The coarse structured mesh (around 172,000 cells), however, only matches the solutions up to an angle of 6° ; at higher angles, it predicts smaller lift and larger drag coefficients. The closed airfoil is further investigated in this work. This geometry is used to determine if predictions of a low-resolution, but high-quality mesh can still match with the medium and fine grid data. The second goal is to relate the solution accuracy and convergence with grid parameters and

quality metrics. All meshes of this work were generated using Pointwise and predictions were compared with solutions of the fine structured grid (containing 3M cells). Cobalt reports an averaged grid quality of 99.74 in a range of zero to 100 for this fine grid.

Figure 5 shows that CFD solutions of the open-inlet airfoil largely depend on the grid resolution. Coarse and medium meshes (containing around 452,000 and 548,000 cells) were generated from a low-density inviscid grid and CFD data using these grids do not match with fine meshes data (containing around 943,000, 1.78 million, and 2.45 million cells). Figure 5 shows that solutions do not change with grid density for the grids that have more than 1.78 million cells. The open-inlet airfoil is also used in this work. The coarse meshes, with different grid generation methods, are tested in Cobalt and the results are compared to the fine mesh (1.78M cells) data in Ref. 21. This grid has a Cobalt quality of 99.83. The meshing study is performed on both outside and inside domains. The effects of meshing on the solution accuracy and convergence are investigated.

V. Results and Discussion

For the sake of convenience, the closed and open inlet grids are labeled “CG” and “OG”, respectively. All CFD simulations were performed using the Spalart-Allmaras (SA) turbulence model and were run on the Cray XE6 machine at the Engineering Research Development Center (ERDC). The freestream velocity in all simulations was fixed at Mach 0.1 and the Reynolds number is 1.4×10^6 at standard sea level conditions. The simulation were performed for an angle-of-attack sweep from zero to ten degrees with one degree increment. In all simulations, second-order accuracy in time, 3 Newton sub-iterations, and 20,000 iterations with a time step of 10^{-4} seconds were used. The last 10,000 iteration values were averaged to obtain overall lift and drag coefficients.

All grids were run in Cobalt and errors in the force coefficients from the predictions of fine meshes are estimated. Specifically, the error norm of lift coefficient (C_L), drag coefficient (C_D), and lift to drag ratio (L/D) is defined as:

$$err = \frac{\sqrt{\frac{1}{N_i} \sum_{j=1}^{N_i} (y_j^{\text{NewGrid}} - y_j^{\text{FineGrid}})^2}}{|y^{\text{FineGrid}}(\text{max}) - y^{\text{FineGrid}}(\text{min})|} \times 100 \quad (19)$$

where $y = [C_L, C_D, L/D]$; N_i is number of angles of attack which is 11 in this work. The error norm is also found for the maximum lift coefficient ($C_{L\text{max}}$) as

$$err2 = \frac{C_{L\text{max}}^{\text{NewGrid}} - C_{L\text{max}}^{\text{FineGrid}}}{C_{L\text{max}}^{\text{FineGrid}}} \times 100 \quad (20)$$

A. Closed-Inlet Airfoil

A medium size grid (named CG1) was generated with details given in Table 1. The grid was generated layer by layer using an elliptic extrusion method starting from the walls. The method stops when the new grid layer reaches a total height of 200m. The outer edges of the cells, at the final layer, define the freestream boundary. The coarse grid used in Ref. 21 was also modified to have exactly the same number of grid points and spacings on the walls as the CG1 mesh. This new grid (named CG2), however, was generated using a multi-block method with an algebraic grid generator applied to each block. CG2 grid details are also given in Table 1. Table 1 confirms that CG1 and CG2 grids have nearly equal number of cells. The overview of grids near trailing edge is shown in Figure 6.

Table 2 compares y^+ , Cobalt grid quality, and the error norms on the CG1 and CG2 grids. While both grids have approximately the same resolution, y^+ , and grid quality, the errors from CG1 are one order of magnitude less than CG2 grid. In more details, Figure 7 compares the lift and drag coefficients of CG1 and CG2 grids with the fine grid data. The comparisons show that the CG1 grid perfectly matches with the fine

grid predictions, however, CG2 predictions do not match everywhere. A question that arises is why these grids, both structured, with the same y^+ , grid quality, and resolution lead to different answers to the exact same problem.

Prior to answering this question, let's first examine the convergence of solution of CG1 and CG2 grids. Figure 8 shows the convergence histories of the density residual ($D\rho/Dt$) for the CG1 and CG2 grids as well as the fine mesh containing 3M cells. From this figure, it can be seen that both the CG1 and CG2 grids reached converged values with approximately three orders of magnitude reduction in the density residual. Figure 8 also indicates that both grids exhibit very similar convergence behavior. Since CG1 and CG2 have the same quality and resolution, a preliminary conclusion is that solution convergence in Cobalt is related to the grid quality and the resolution; this will be further examined later for more grids. The fine mesh quality in Cobalt is 99.74 slightly higher than CG1 and CG2; also it is a very high spatial resolution grid. As expected, Figure 8 shows that the fine mesh has better convergence than other grids.

Now, in attempting to answer the aforementioned question, the reader is referred again to the mesh overviews shown in Figure 6. Detailed visualization of the cells around the trailing edge reveals that CG1 has better wall orthogonality (straightness), smoothness, and skewness compared to CG2. Many cells in CG2 are highly skewed; besides most mesh lines are not orthogonal to the walls. However, Cobalt's overall grid quality is very similar for both grids. The grid quality plots of CG1 and CG2 (around the trailing edge) can also be seen in Figures 9 (a) and (b). Note that white cells in the figures indicate high grid quality (above 99). Figure 9 (b) shows that most CG2 cells in Cobalt have high quality while they were expected to have low quality because of the poor flow alignment and skewness.

Grid smoothness, skewness, and the wall orthogonality values are also shown in Figure 9. This figure shows that CG1 cells are well-shaped with good smoothness and 90 degrees wall angles. Comparing these plots with Cobalt grid quality pictures reveals that Cobalt grid quality is related to the grid smoothness, but not the skewness or the wall orthogonality. Figure 10 shows the same correspondence for the cells near the leading edge. CG2 cells at the leading edge have slightly better smoothness than CG1, but it has highly skewed cells. Figure 10 shows that Cobalt's quality (at the leading edge) is better for CG2 compared to CG1 cells. This again confirms that Cobalt grid quality does not change with the skewness or wall orthogonality. This means that a high grid quality in Cobalt corresponds to good smoothness which would improve the convergence but it does not necessarily provide better accuracy. The flow solutions at the CG1 and CG2 grids will be presented later in this section.

Four new grids (CG10 - CG13) were generated around the closed-inlet airfoil by the normal extrusion of the wall using an elliptic mesh generator. The edge lengths of these grids are about half of the edges in CG1 and CG2 grids. All grids are structured and contain around 120,000 cells. The near-wall grid spacing (Δ_{s1}) is 4×10^{-5} m for these grids which makes the overall y^+ near one. The difference between these four grids is only due to the farfield length(l); it varies from 25 to 100 chord lengths. Grid details and errors (from the fine mesh data) are given in Tables 1 and 2.

Figure 11 (a) shows that CG10-CG13 grids have very similar convergence behavior; again, because these grids have the same resolution and quality. Figure 11 (a) shows that the farfield length had no considerable effect on the convergence rate in Cobalt. Figure 11 (b) also shows the error trends with farfield length for grids CG10 - CG13. Increasing the farfield length above 50 chord lengths does not change much the C_L , C_D and C_{Lmax} errors; Figure 11 (b) shows that L/D predictions can be improved by making the farfield boundary bigger but its impact becomes smaller above $50c$. For all subsequent grids, a farfield length of 50 chord will therefore be used.

CG20-CG21 grids were generated by similar mesh generation methods, however, the near-wall grid spacing (Δ_{s1}) varies in these grids. The convergence data of these grids (CG20 - CG21) are shown in Figure 12 (a) which shows the convergence improves as y^+ decreases from one to around 0.26 (CG11 in this figure has $y^+ = 1$). The solution accuracy is also improved with decreasing y^+ as shown in Figure 12 (b). Figure 13 compares the lift and drag coefficient predictions of CG21 grid ($y^+=0.2663$ and containing 134,000 cells) with predictions from CG1 ($y^+=0.2663$ and containing 341,000 cells). The results show that CFD data of the coarse grid match very well with the medium grid data. Note that CG1 data also match with CFD data of the fine grid. These results show that a grid size of around 134,000 cells and y^+ of 0.26 with well-shaped cells will match the fine data of Ref. 21.

Three unstructured meshes (CG30-32) were also considered; these meshes were generated by the Delaunay tetrahedralization and have anisotropic cells near the wall with a growth rate of 1.1. These grids are very similar, except that they have different initial spacing near the wall. Grid details and errors are given in

Tables 1 and 2. These grids have around 115,000 cells and have grid quality above 99. Figure 14 compares CG21 (structured) with the CG32 (unstructured). The anisotropic cells near the wall can be seen in this figure. Note that anisotropic tetrahedral layers are not constant everywhere; the local extrusion at each point would stop if the cell size become close to the size of outside isotropic cells.

Figure 15 compares the Cobalt quality plot of CG32 with the Pointwise skewness quality picture of CG32. Figure 15(b) shows that the cells near the wall are extremely skewed, but Cobalt considers these cells high-quality ones because of the good grid smoothness. The convergence history of CG1, CG21, and CG32 are plotted in Figure 16. Despite having a poor skewness near the wall, CG32 has very similar convergence behavior to CG21 which is a structured grid. This again confirms that Cobalt convergence does not change much with the skewness quality. CG1 has better convergence than the other grids because it has a high-resolution compared with CG21 and CG32.

Although CG32 and CG21 have similar quality and convergence, Table 2 shows that CG32 has much larger errors in the lift and drag coefficients than CG21. In more details, Figure 17 compares the lift and drag values for grids of CG1, CG21, and CG32. Figure 17 shows that CG32 match well with CG21 and CG1 data at small angles of attack; however, for angles above 6° , CG32 lift overestimates CG21/CG1 data and CG32 underestimates drag. Finally, for the structured grids of CG11, CG20, and CG21, Table 2 shows that the accuracy is improved by decreasing y^+ from one to 0.26; this, however, does not apply to the unstructured grids. Decreasing the initial spacing makes the cells near the wall more skewed assuming the wall spacing is unchanged. Poor skewness would impact the solution accuracy.

The final closed grids considered are of hybrid type with prismatic layers near the wall and isotropic cells elsewhere. Three hybrid grids CG40, CG41, and CG42, were generated. The prismatic layers were generated by the wall normal extrusion using an elliptic solver. The outer domain is then meshed by the Delaunay tetrahedralization. These grids are much coarser than the structured grids of CG10 to CG21. Grid details and errors are again given in Tables 1 and 2. The main difference between these grids is the number of prism layers. Figure 18 shows the mesh overview of CG42 with 75 prism layers. The effect of the number of prism layers on the errors can be seen in Figure 19 which shows the accuracy is significantly improved by increasing the layers from 25 to 50; however, the accuracy does not change much by increasing layers from 50 to 75. Figure 20 also compares the lift and drag coefficients of the hybrid CG42 mesh with predictions of CG1 and CG21 grids. The results show that predictions from a hybrid grid with 75 prism layer still match quite well with expected data.

Finally, Figure 21 shows the flow solution on the CG1, CG2, CG32, and CG42 grids at nine degrees angle of attack. For all grids at $\alpha = 9^\circ$, the boundary layer is separated from the upper surface and a clockwise-rotating eddy is formed. Figure 21 shows that eddy size and pressure coefficients are very similar for the CG1 and CG42 grids; these grids have well-shaped cells with 90 degrees wall angles closed to the wall. Eddies predicted by the CG2 and CG32 are, however, bigger and smaller than CG1 eddy, respectively. Therefore, CG2 underestimate and CG32 overestimate the lift predicted by OG1. Note that the CG2 is structured grid with poor skewness and wall orthogonality; CG32 has highly skewed anisotropic cells at the wall as well.

B. Open-Inlet Airfoil

The computational domain of this geometry consists of two parts corresponding to the outside and inside of the airfoil. These domains are meshed separately in this work. The first grids considered are structured; the outside mesh was generated by the wall normal extrusion and the inside mesh is an algebraic mesh nearly uniform in spacing even at the inside walls. These meshes are named OG1- OG5. All these grids have the same inside mesh containing around 278,000 cells. OG1- OG3 have an initial spacing of 4×10^{-5} m at the outside walls but they have different number of layers of constant spacing. OG4 and OG5 have 5 layers of constant spacing at the outside walls but the initial spacing of these meshes are 2×10^{-5} m and 1×10^{-5} m, respectively. The OG1 mesh is shown in Figure 22. OG1 has 25 layers of constant spacing at the outside walls which can easily be seen in Figure 22.

OG1 to OG5 grids contain around 400,000 cells. Figure 23 (a) shows the convergence histories of OG1, OG2, and OG3 grids compared with the hybrid fine mesh (1.7M cells) convergence. The convergence comparisons show that all coarse grids converged to the same values; again due to having similar resolution and quality. In comparison to the closed-inlet airfoil convergence plots, Figure 23 (a) shows that the open-inlet take a longer time to converge. Also, Figure 23(a) shows that the fine grid convergence is not significantly different from these coarse grids.

The effects of the number of constant-spacing layers at the wall (N_s) on the errors are shown in Figure 23 (b). The results show that N_s has a small effect on the open-inlet solutions. In more details, the lift and drag coefficients of OG1, OG2, and OG3 grids are compared with the fine mesh predictions in Figure 24. The lift and drag coefficients are split into the inner and outer surfaces. Notice that inner lift does not change with the angle of attack; Ghoreyshi et al.²¹ showed that flow is relatively stationary inside with C_p near one almost everywhere. Figure 24 (b), however, shows that the outer surface has negative drag before stall angle and the inner surface has very large drag. The comparison plots of Figure 24 show that coarse grids with uniform spacing inside match very well with the fine mesh force coefficients at inside and outside walls.

OG2, OG4, and OG5 have around 278,000 cells inside and very similar grids outside; in these grids $N_s = 5$ and the growth rate is 1.1. However, the initial grid spacing is different; y^+ values of these grids are given in Table 4 and range from one for the OG2 to 0.23 for the OG5. The effects of y^+ on the errors are shown in Figure 25 and compared with trends of closed-inlet solutions. Figure 25 shows that the errors of the open-inlet grids are slightly reduced by decreasing y^+ , however, the errors of all y^+ values considered are small and less than 2%. On the other hand, the solution accuracy of the closed-inlet grid significantly changes with y^+ . A possible explanation of why the open-inlet geometries is less sensitive to y^+ than closed-inlet can be offered from the flow solutions. Figure 26 (a) shows the flow streamlines of OG5 mesh at $\alpha = 9^\circ$. At moderate to high angles of attack, flow enters the open section of the open-inlet and then exits from the upper and lower surfaces. This makes flow separated over the upper and lower surface right at the inlet. The closed-inlet geometry at high angles of attack also shows a separated flow region right at the inlet due to the inlet sharp angle; however, the separated region is significantly smaller than those occurred on the open-inlet airfoils. In the closed-inlet, the separated eddy size largely depends on the predicted boundary layer at the inlet wall surface; this makes the flow solutions very sensitive to the initial grid spacing and viscous layer used at the inlet surface.

OG5, OG10, OG11, OG12 grids were used to study the effect of inside mesh resolution on the overall solutions. All these grids have very similar meshes outside but inside mesh changes from 278,000 to 22,000 cells. This is achieved by reducing the inside wall grid dimensions. OG12 grid is shown against OG5 in Figure 27. Figure 28(a) shows that the density residual on the OG12 (coarse grid) is not reduced as low as OG5 and the fine mesh; however, the accuracy is still as good as others as shown in Figure 28(b) which shows OG12 errors from the fine mesh are less than 1%. This means that the open-inlet solution is not very sensitive to the number of cells inside.

To investigate the inside mesh type on the solution, OG20 and OG21 grids were also generated; these grids again have a structured mesh outside as the previous meshes, but the inside was meshed by the Delaunay tetrahedralization. OG20 has only 9,800 tetrahedra cells inside; the grid is shown in Figure 29(a). Table 4 and Figure 30 show that OG20 with coarse tetrahedra cells inside still match with the fine data. Therefore solutions do not depend much on the inside cell resolution or cell type. Figure 26 (b) shows the flow solutions of OG20 at $\alpha = 9^\circ$. This figure shows that the flow inside the airfoil is stationary almost everywhere as predicted by other meshes; therefore the flow solution should not change much with inside mesh resolution.

The OG22 mesh has unstructured cells inside and outside. The outside is meshed by the Delaunay tetrahedralization and has anisotropic layers at the wall. Inside cells are isotropic tetrahedra cells. The mesh and solutions are shown in Figure 29(b) and Figure 30, respectively. Figure 30 shows that the forces on the outer surface of the airfoil and therefore total lift and drag do not match with fine data everywhere. This is probably due to having highly skewed cells near the outer walls. The flow solution on the OG22 grid is also shown in Figure 26 (c) for at $\alpha = 9^\circ$. The figure shows that the flow is separated from the upper surface and a clockwise-rotating eddy is formed at this angle, however, the eddy size and septation might do not match with those predicted by OG5 and OG20 grids. Note that the eddy formed over the open-inlet airfoil is much bigger than those predicted over the closed-inlet airfoil at $\alpha = 9^\circ$.

The final grid, OG40, is a hybrid mesh outside and unstructured inside. The viscous grid on the outside wall was generated by the wall normal extrusion; it has 75 layers. The rest of outside domain is meshed by the Delaunay mesh generator. An overview of the grid is shown in Figure 31. The convergence solution on this grid is plotted in Figure 32 which shows the residual reduction for the OG40 and OG20 meshes are the same; however residual reduction of these meshes is not as low as OG1 or the fine mesh. On the other hand, the OG20 grid (with unstructured cells inside) and OG40 hybrid grid exhibit a faster convergence rate than the OG1 structured grid. The lift and drag coefficients of the OG40 are also compared with the fine and OG1 mesh in Figure 33 which shows that the hybrid grid matches well with data from the other grids data; there are very small discrepancies in lift coefficients in the post-stall region. Figure 26 (d) shows the

flow solution over this grid at $\alpha = 9^\circ$. Note that the eddy size at this angle is bigger than the viscous layer generated with 75 prismatic layers; this probably explains small discrepancies between this grid and those of the structured type.

VI. Conclusions

This paper provides an overview of the grid quality and resolution effects on the aerodynamic modeling of ram-air parachute canopies. The CFD simulations were performed using the Cobalt flow solver on two dimensional canopy sections with open and closed inlets. The simulation results show that Cobalt grid quality (ranging from zero to 100) depends mainly on the mesh smoothness, but not the skewness or the wall orthogonality. Cobalt convergence is improved with increasing grid resolution, grid quality (smoothness) and decreasing initial grid spacing at the wall (y^+). The results showed that while a high quality grid of Cobalt leads to a better convergence, it does not always lead to better accuracy. The solution accuracy will change with grid resolution and smoothness, as well as skewness and the wall orthogonality.

The results of this work showed the solutions of coarse structured and hybrid grids (around 100,000 cells) can match well with prediction of fine meshes containing a few million cells. These coarse grids have appropriate y^+ values, good smoothness, skewness, and wall orthogonality. While unstructured meshes with anisotropic cells near the wall have very good grid quality in Cobalt, they have the worst accuracy between considered grids because of poor skewness at the walls. The results also showed that in comparison to the closed inlets, the open geometry solutions are less sensitive to the initial grid spacing and number of constant spacing layer at the outside walls. Also, the solutions do not change with inside mesh resolution and type. However, a mesh with anisotropic layers at the outside walls have again the worst accuracy between considered grids.

The results of two-dimensional airfoils, considered in this work, can be easily generalized to three-dimensional wings. For example, a high quality 3D mesh can be created from spanwise extrusion of a high quality 2D mesh. Our future work will expand the results to include meshes around three-dimensional wings with open inlet, deflected trailing edges, and bleed-air spoilers. The experiments of these wings are underway at the USAFA subsonic wind tunnel.

VII. Acknowledgements

Mehdi Ghoreyshi and Jürgen Seidel are supported by USAFA; their financial support is gratefully acknowledged. Acknowledgements are expressed to the Department of Defense High Performance Computing Modernization Program (HPCMP) and ERDC for providing computer time. The authors appreciate the support provided by the Natick Soldier Research Development and Engineering Center (NSRDEC) Airdrop Technology Team and the High Performance Computing Research Center at USAFA.

This material is based in part on research sponsored by the US Air Force Academy under agreement number FA7000-13-2-0009. The U.S. Government is authorized to reproduce and distribute reprints for Governmental purposes notwithstanding any copyright notation thereon. The views and conclusions contained herein are those of the authors and should not be interpreted as necessarily representing the official policies or endorsements, either expressed or implied, of the US Air Force Academy or the U.S. Government.

References

- ¹Liseikin, V. D., *Grid Generation Methods (Scientific Computation)*, Springer, Second Edition, 2010.
- ²Anderson, J. D., *Modern Compressible Flow*, McGraw-Hill, Second Edition, 1990.
- ³McCormick, S. F., *Multilevel Adaptive Methods for Partial Differential Equations*, Society of Industrial and Applied Mathematics, 1989.
- ⁴Gu, X., Schock, H. J., Shih, T. I.-P., Hernandez, E. C., Chu, D., Keller, P. S., and Sun, R. L., "Grid-Quality Measures for Structured and Unstructured Meshes," AIAA Paper 2001-0665, January 2001.
- ⁵Thompson, J. F., Soni, B. K., and Weatherill, N. P., *Handbook of Grid Generation*, CRC Press, 1999.
- ⁶Knupp, P. and Steinberg, S., *Fundamentals of Grid Generation*, CRC Press, 1994.
- ⁷Henne, P. A., *Applied Computational Aerodynamics*, American Institute of Aeronautics and Astronautics, 1990.
- ⁸Baker, T. J., "Three Decades of Meshing; A Retrospective View," AIAA Paper 2003-3563, June 2003.
- ⁹Sarrate, J. and Staten, M., *Proceedings of the 22nd International Meshing Roundtable*, Springer, 2014.
- ¹⁰Cheng, S.-W., Dey, T. K., and Shewchuk, J. R., *Delaunay Mesh Generation*, CRC Press, 2013.

¹¹Leondes, C. T., *Structural Dynamic Systems Computational Techniques and Optimization, Volume 1*, Overseas Publishers Association, 1998.

¹²Michal, T. and Cary, A., “Unstructured Grid Extrusion for Viscous Flow Simulations,” AIAA Paper 2001-0444, January 2001.

¹³Chalasan, S. and Thompson, D., “Quality Improvements in Extruded Meshes Using Topologically Adaptive Generalized Elements,” *International Journal for Numerical Methods in Engineering*, Vol. 60, 2004, pp. 1139–1159.

¹⁴Ito, Y. and Nakahashi, K., “Unstructured Hybrid Grid Generation Based on Isotropic Tetrahedral Grids,” AIAA Paper 2002-0861, January 2002.

¹⁵Ghoryeshi, M., Jirasek, A., and Cummings, R. M., “Computational Investigation into the Use of Response Functions for Aerodynamic Loads Modeling,” *AIAA Journal*, Vol. 50, No. 6, 2012, pp. 1314–1327.

¹⁶Ghoryeshi, M., Post, M. L., and Cummings, R. M., “CFD Calculation of Aerodynamic Indicial Functions for a Generic Fighter Configuration,” *ITEA Journal of Test and Evaluation*, Vol. 33, No. 6, 2012, pp. 348–364.

¹⁷Ghoreyshi, M., Cummings, R. M., DaRonch, A., and Badcock, K. J., “Transonic Aerodynamic Loads Modeling of X-31 Aircraft Pitching Motions,” *AIAA Journal*, Vol. 51, No. 10, 2013, pp. 2447–2464.

¹⁸Ghoreyshi, M. and Cummings, R. M., “Unsteady Aerodynamics Modeling for Aircraft Maneuvers: A New Approach Using Time-Dependent Surrogate Modeling,” *Aerospace Science and Technology*, Vol. 39, 2014, pp. 222–242.

¹⁹Tyssel, L., “Hybrid Grid Generation for Complex 3D Geometries,” Proceedings of the 7th International Conference on Numerical Grid Generation in Computational Field Simulation, 2000, pp. 337–346.

²⁰Tyssel, L., “The TRITET Grid Generation System,” International Society of Grid Generation (ISGG),” Proceedings of the 10th International Conference on Numerical Grid Generation in Computational Field Simulations, 2000.

²¹Ghoreyshi, M., Seidel, J., Bergeron, K., Jirasek, A., Lofthouse, A. J., and Cummings, R. M., “Prediction of Aerodynamic Characteristics of a Ram-Air Parachute,” AIAA Paper 2014-2831, June 2014.

²²Bergeron, K., Jurgen, S., Ghoreyshi, M., Jirasek, A., Lofthouse, A. J., and Cummings, R. M., “Numerical Study of Ram Air Airfoils and Upper Surface Bleed-Air Control,” AIAA Paper 2014-2832, June 2014.

²³Strang, W. Z., Tomaro, R. F., and Grismer, M. J., “The Defining Methods of Cobalt: A Parallel, Implicit, Unstructured Euler/Navier-Stokes Flow Solver,” AIAA Paper 1999-0786, January 1999.

²⁴Gottlieb, J. J. and Groth, C. P. T., “Assessment of Riemann Solvers For Unsteady One-dimensional Inviscid Flows of Perfect Gasses,” *Journal of Computational Physics*, Vol. 78, No. 2, 1988, pp. 437–458.

²⁵Tomaro, R. F., Strang, W. Z., and Sankar, L. N., “An Implicit Algorithm For Solving Time Dependent Flows on Unstructured Grids,” AIAA Paper 1997-0333, 1997.

²⁶Tomaro, R. F., Strang, W. Z., and Wurtzler, K. E., “Can Legacy Codes Scale on Tens of Thousands of PEs or Do We Need to Reinvent the Wheel?” 2012 High Performance Computing Modernization Program Contributions to DoD Mission Success, pp. 231-236, September 2012.

²⁷Spalart, P. R. and Allmaras, S. R., “A One Equation Turbulence Model for Aerodynamic Flows,” AIAA Paper 1992-0439, January 1992.

²⁸Spalart, P. R. and Shur, M. L., “On the Sensitization of Turbulence Models to Rotation and Curvature,” *Aerospace Science and Technology*, Vol. 1, 1997, pp. 297–302.

²⁹Spalart, P. R., Jou, W.-H., Strelets, M., and Allmaras, S. R., “Comments on the Feasibility of LES for Wings, and on a Hybrid RANS/LES Approach,” 1997, In Proceedings, 1st AFSOR International Conference on DNS/LES, Greyden Press, Columbus, OH, pp. 137–147.

³⁰“Cobalt User’s Manual,” Cobalt Solutions, February 11, Cobalt Version 6.0, 2013.

³¹Dannenhoffer, J. F., “Correlation of Grid Quality Metrics and Solution Accuracy for Supersonic Flows,” AIAA Paper 2012-0610, January 2012.

³²McDaniel, D. R., *Deformation of Viscous CFD Meshes for Aeroelastic and S&C Applications*, Phd dissertation, Department of Mechanical and Aerospace Engineering, University of Colorado at Colorado Springs, November 2010.

³³Rumsey, C. L. and Slotnick, J. P., “Overview and Summary of the Second AIAA High Lift Prediction Workshop,” AIAA Paper 2014-0747, January 2014.

³⁴Mavriplis, D. J., Vassberg, J. C., Tinoco, E. N., Mani, M., Brodersen, O. P., Eisfeld, B., Wahls, R. A., Morrison, J. H., Zickuhr, T., Levy, D., and Murayama, M., “Grid Quality and Resolution Issues from the Drag Prediction Workshop Series,” AIAA Paper 2008-0930, January 2008.

³⁵Maddock, I., Harby, A., Kemp, P., and Wood, P. J., *Ecohydraulics: An Integrated Approach*, John Wiley & Sons, 2013.

³⁶Alter, S. J., “A Structured-Grid Quality Measure for Simulated Hypersonic Flows,” AIAA Paper 2004-0612, January 2004.

³⁷Morton, S. A., McDaniel, D. R., Sears, D. R., Tillman, B., and Tuckey, T. R., “Kestrel: A Fixed Wing Virtual Aircraft Product of the CREATE Program,” AIAA Paper 2009-0338, January 2009.

³⁸Benney, R. J., Krainski, W. J., Onckelinx, C. P., Delwarde, C. C., Mueller, L., and Vallance, M., “NATO Precision Airdrop Initiatives and Modeling and Simulation Needs,” RTO-MP-AVT-133 Technical Report, October 2006.

³⁹Bergeron, K., Ward, M., and Costello, M., “Aerodynamic Effects of Parafoil Upper Surface Bleed Air Actuation,” AIAA Paper 2012-4737, August 2012.

⁴⁰Lingard, J. S., “Precision Aerial Delivery Seminar Ram-Air Parachute Design,” 13th AIAA Aerodynamic Decelerator Systems Technology Conference, Clearwater Beach, May 1995.

Table 1. Closed grid details. In OG1 and OG2, $N_s=7$, for all other grids $N_s=0$. In all grids GR =1.1.

Grid	Type	Method	Δ_{s1}	l/c	# Cells
Fine	STR	Multi-block, algebraic	1e-5	50	3,141,000
CG1	STR	Normal extrusion, elliptic	1e-5	100	341,850
CG2	STR	Multi-block, algebraic	1e-5	100	324,570
CG10	STR	Normal extrusion, elliptic	4e-5	25	115,320
CG11	STR	Normal extrusion, elliptic	4e-5	50	120,900
CG12	STR	Normal extrusion, elliptic	4e-5	75	124,620
CG13	STR	Normal extrusion, elliptic	4e-5	100	128,340
CG20	STR	Normal extrusion, elliptic	2e-5	50	127,410
CG21	STR	Normal extrusion, elliptic	1e-5	50	133,920
CG30	UNSTR	Delaunay, anisotropic viscous layers	4e-5	50	101,894
CG31	UNSTR	Delaunay, anisotropic viscous layers	2e-5	50	114,970
CG32	UNSTR	Delaunay, anisotropic viscous layers	1e-5	50	128,564
CG40	HYBRID	Delaunay, 25 prismatic viscous layers	1e-5	50	55,324
CG41	HYBRID	Delaunay, 50 prismatic viscous layers	1e-5	50	77,754
CG42	HYBRID	Delaunay, 75 prismatic viscous layers	1e-5	50	100,842

Table 2. Closed grid solution details.

Grid	y^+	Quality	err %			
			C_L	C_D	L/D	C_{Lmax}
CG1	0.2663	98.62	0.1484	0.1276	0.2209	0.1183
CG2	0.2339	98.81	1.1504	2.0752	5.6311	-1.7914
CG10	1.074	99.14	1.8921	2.9175	8.1312	-1.7116
CG11	1.074	99.15	1.7397	2.3424	5.0274	-1.6729
CG12	1.074	99.16	1.7155	2.2623	4.4330	-1.6793
CG13	1.074	99.19	1.7045	2.2196	4.0466	-1.6824
CG20	0.5336	99.12	1.0534	1.1167	2.7766	-1.0541
CG21	0.2663	98.99	0.8772	0.7775	2.2576	-0.8549
CG30	0.7260	99.83	0.3247	1.8036	4.3489	0.3532
CG31	0.3642	99.71	4.3107	5.8003	3.6808	1.4514
CG32	0.1796	99.55	3.5703	4.5855	2.9438	1.6056
CG40	0.2663	98.55	5.2646	7.2829	7.8631	-6.2807
CG41	0.2663	98.97	1.0484	0.5219	1.6164	-0.8507
CG42	0.2663	98.94	0.5906	0.8316	2.1128	-0.5507

Table 3. Open grid details. $l/c = 100$ and $GR = 1.1$ for all grids. UNSTR meshes were generated by the Delaunay tetrahedralization. UNSTR meshes at outside walls have anisotropic viscous layers. OG40 has 75 prismatic viscous layers at the outside walls.

Grid	Outside mesh	Inside mesh	Δ_{s1}	N_s	# Cavity cells	# Total cells
Fine	HYBRID	HYBRID	1e-5	-	-	1,782,199
OG1	STR, elliptic	STR, uniform	4e-5	25	278,620	421,840
OG2	STR, elliptic	STR, uniform	4e-5	5	278,620	403,240
OG3	STR, elliptic	STR, uniform	4e-5	0	278,620	399,520
OG4	STR, elliptic	STR, uniform	2e-5	5	278,620	407,500
OG5	STR, elliptic	STR, uniform	1e-5	5	278,620	416,260
OG10	STR, elliptic	STR, uniform	1e-5	5	120,384	285,028
OG11	STR, elliptic	STR, uniform	1e-5	5	56,000	194,188
OG12	STR, elliptic	STR, uniform	1e-5	5	22,000	148,262
OG20	STR, elliptic	UNSTR	1e-5	5	9,812	137,058
OG21	STR, elliptic	UNSTR	1e-5	5	5,209	136,520
OG22	UNSTR	UNSTR	1e-5	-	5,275	118,202
OG40	HYBRID	UNSTR	1e-5	-	5,275	98,620

Table 4. Open grid solution details.

Grid	y^+	Quality	err %			
			C_L	C_D	L/D	C_{Lmax}
OG1	0.9490	99.66	0.7146	1.1728	1.7029	-0.4407
OG2	0.9495	99.69	0.9527	1.4604	1.9284	-0.5427
OG3	0.9501	99.70	1.2356	1.6935	2.3153	-0.7218
OG4	0.4721	99.66	0.4549	0.5146	0.5746	-0.1788
OG5	0.2360	99.59	0.4232	0.3767	0.4536	-0.1312
OG10	0.2360	99.26	0.4269	0.3506	0.4322	-0.0934
OG11	0.2359	98.85	0.4430	0.4462	0.5599	-0.1770
OG12	0.2357	98.86	0.5402	0.4694	0.8619	-0.4866
OG20	0.2360	98.92	0.4994	1.5627	2.6723	-0.1016
OG21	0.2360	98.91	0.4323	1.8874	3.8378	-0.1263
OG22	0.1599	99.35	3.4452	1.1538	2.6855	1.7791
OG40	0.2364	98.90	1.0078	1.5233	3.2509	0.3833

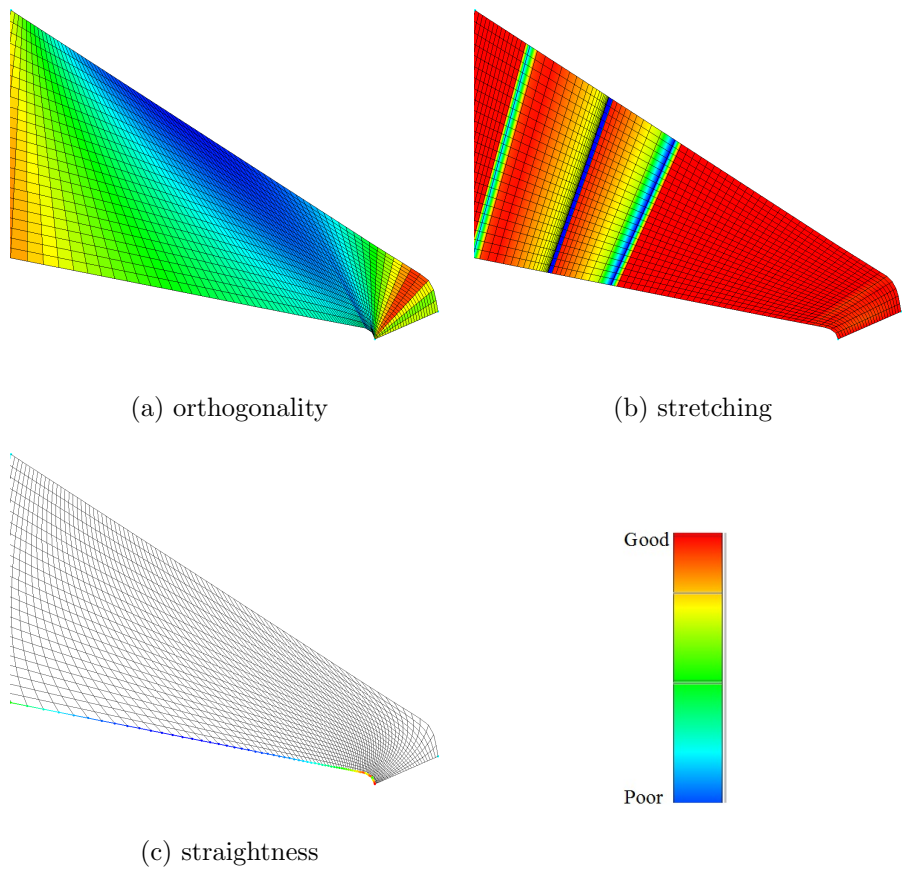
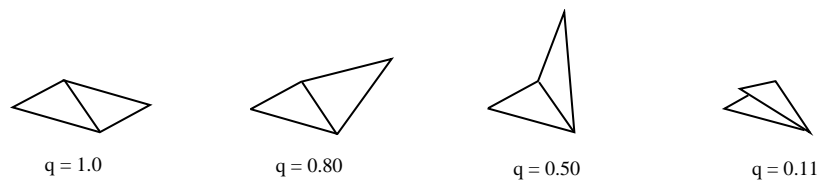
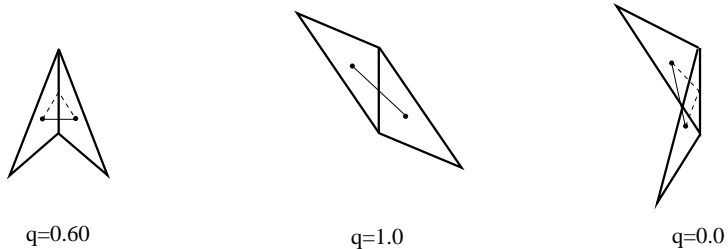
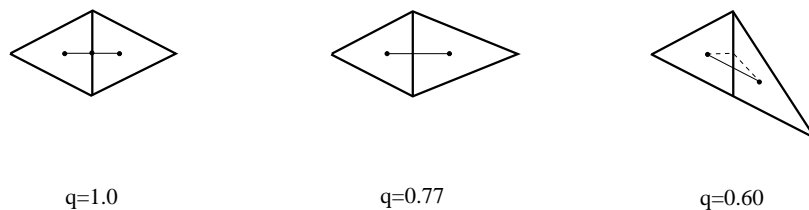


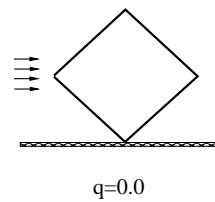
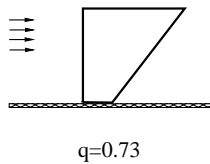
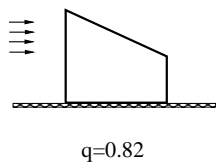
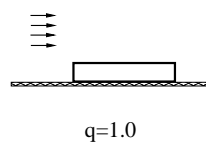
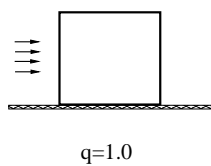
Figure 1. Orthogonality, stretching, and straightness examples for structured grids.



(a) planar quality metric examples



(b) skew-smoothness metric examples



(c) flow alignment metric examples

Figure 2. Planar, skew-smoothness, and flow alignment metric examples from Ref. 32 .

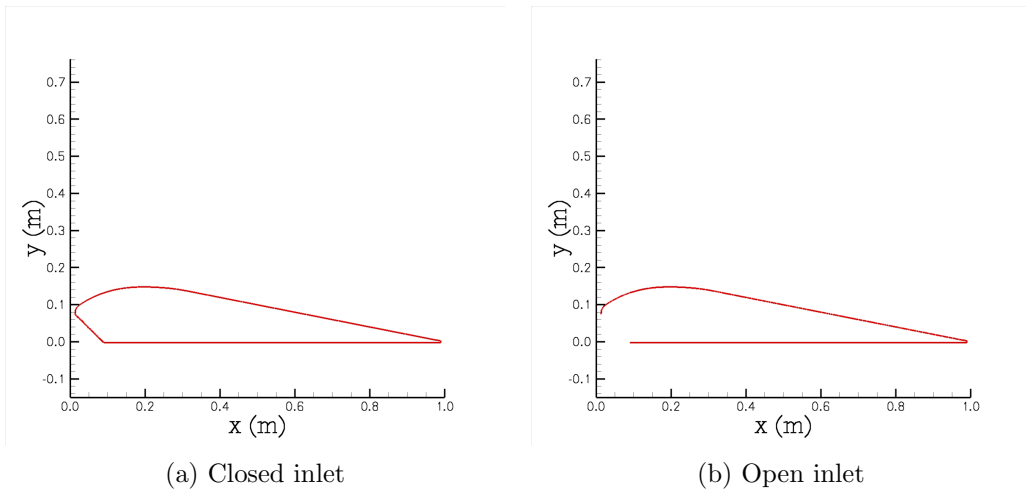


Figure 3. Airfoil geometries for the parachute cases

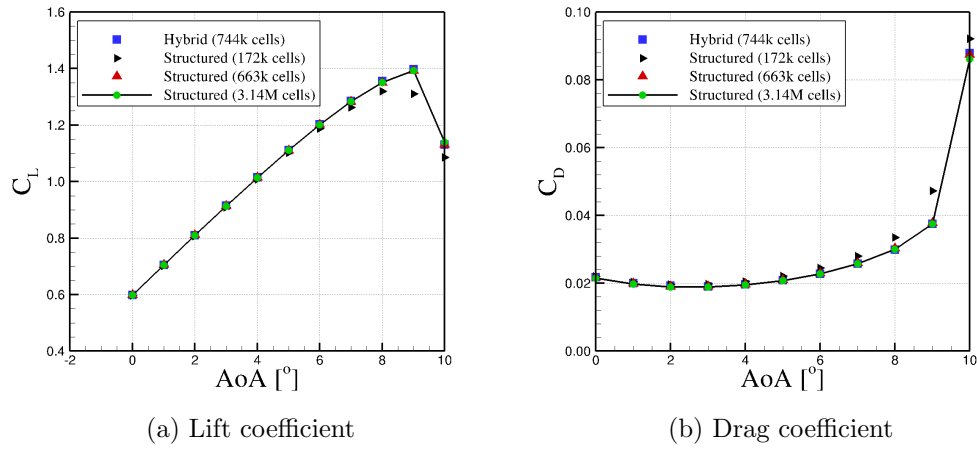


Figure 4. Mesh-independence study of the closed-inlet airfoil.

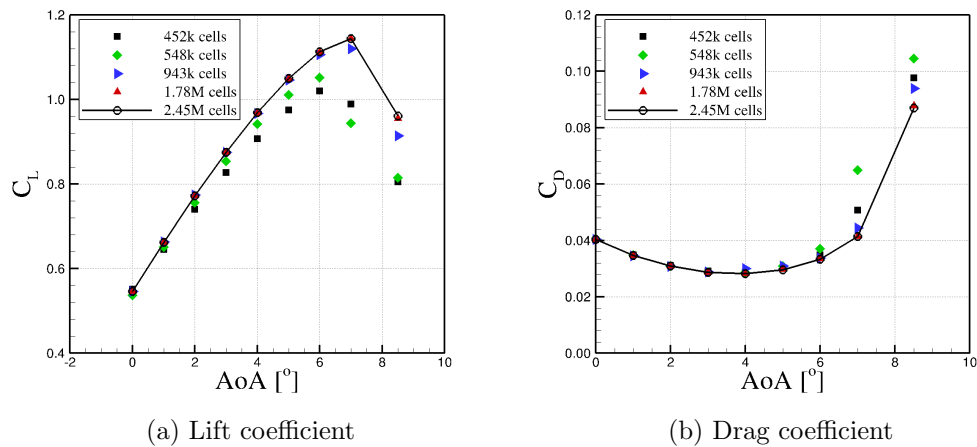
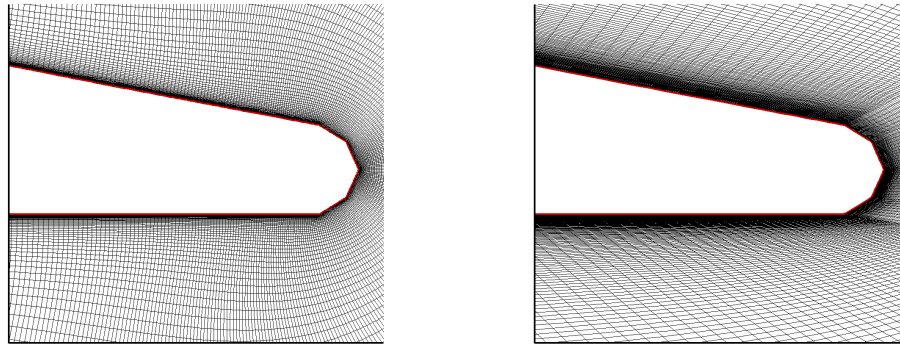


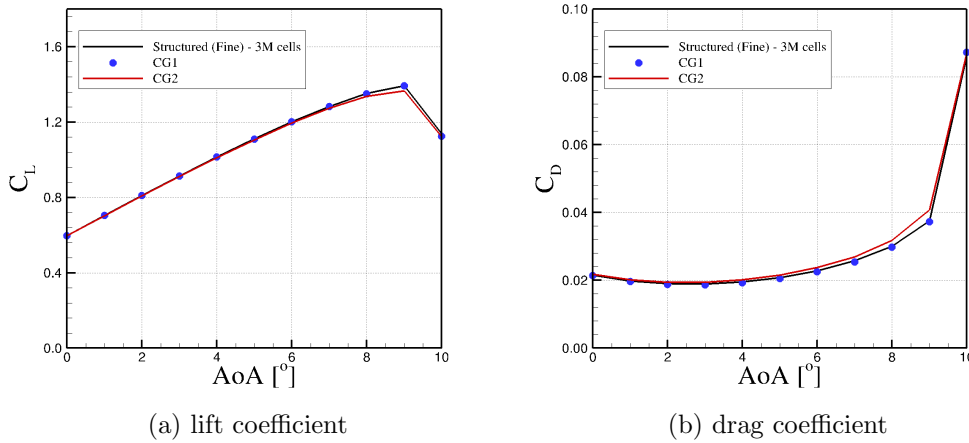
Figure 5. Mesh-independence study of the open-inlet airfoil.



(a) CG1, structured (elliptic mesh)

(b) CG2, multi-block (algebraic mesh)

Figure 6. CG1 and CG2 grids overview.



(a) lift coefficient

(b) drag coefficient

Figure 7. Lift and drag coefficients of CG1 and CG2 grids. The structured fine grid is from Ref. 21.

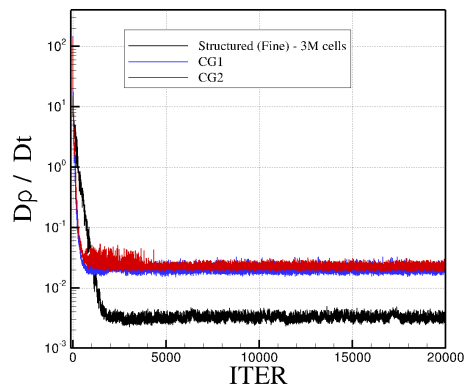
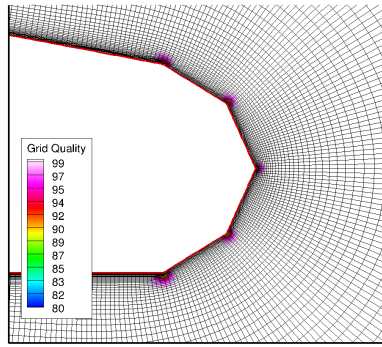
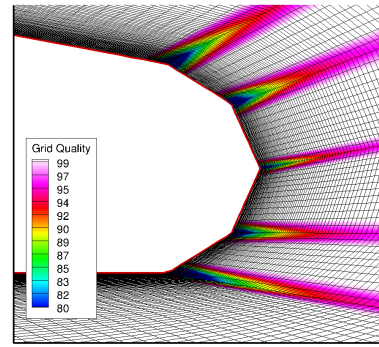


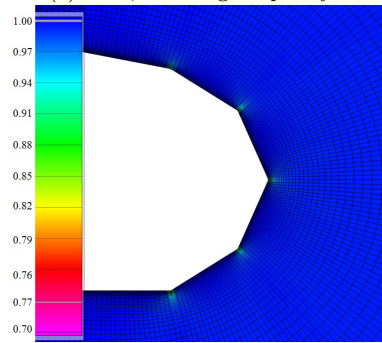
Figure 8. Density residual convergence ($D\rho/Dt$) of CG1 and CG2 grids, where ρ and t denote density and time, respectively. The structured fine grid is from Ref. 21.



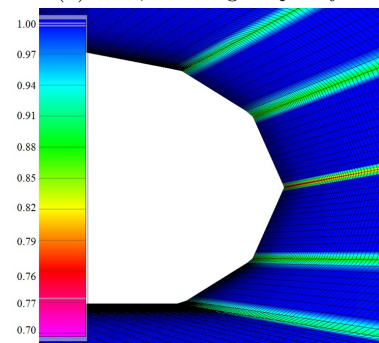
(a) CG1, Cobalt grid quality



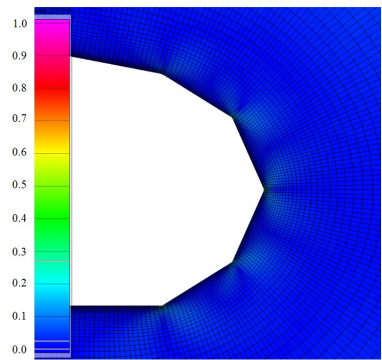
(b) CG2, Cobalt grid quality



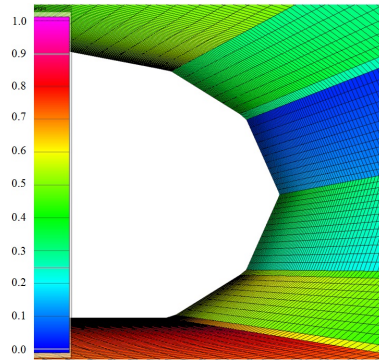
(c) CG1, smoothness



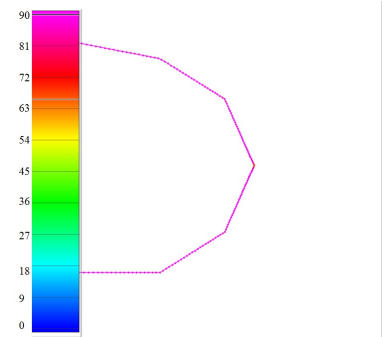
(d) CG2, smoothness



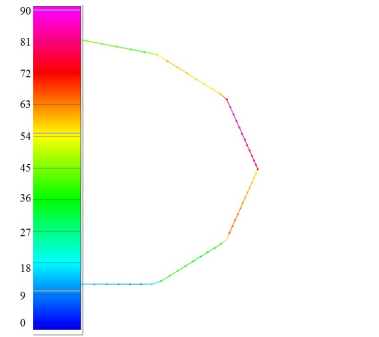
(e) CG1, skewness



(f) CG2, skewness



(g) CG1, wall orthogonality (deg)



(h) CG2, wall orthogonality (deg)

Figure 9. Cobalt grid quality relationship with mesh geometry- Mesh is around trailing edge. In (a) and (b) the white cells have the highest quality.

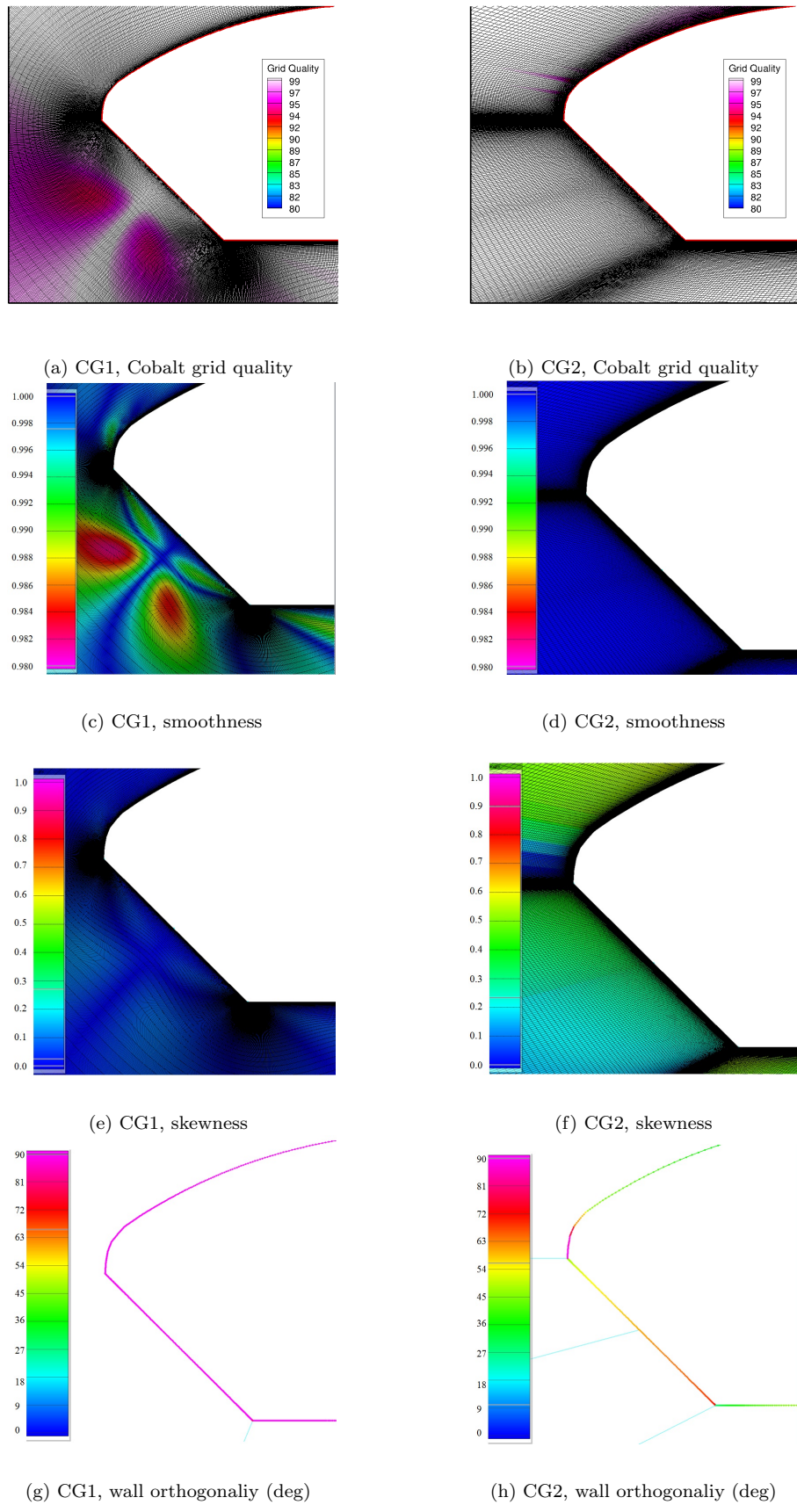


Figure 10. Cobalt grid quality relationship with mesh geometry- Mesh is around leading edge. In (a) and (b) the white cells have the highest quality.

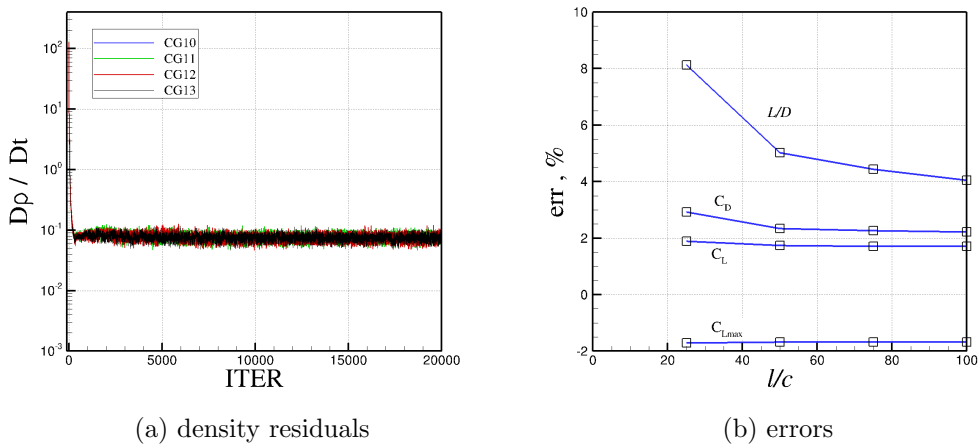


Figure 11. Effects of farfield length (l) on the solution convergence and errors.

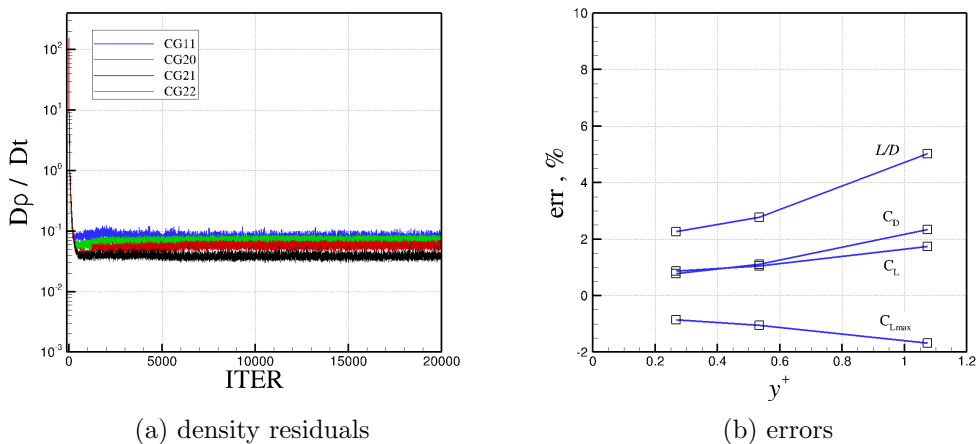


Figure 12. Effects of initial grid spacing (Δ_{s1}) on the solution convergence and errors of structured grids.

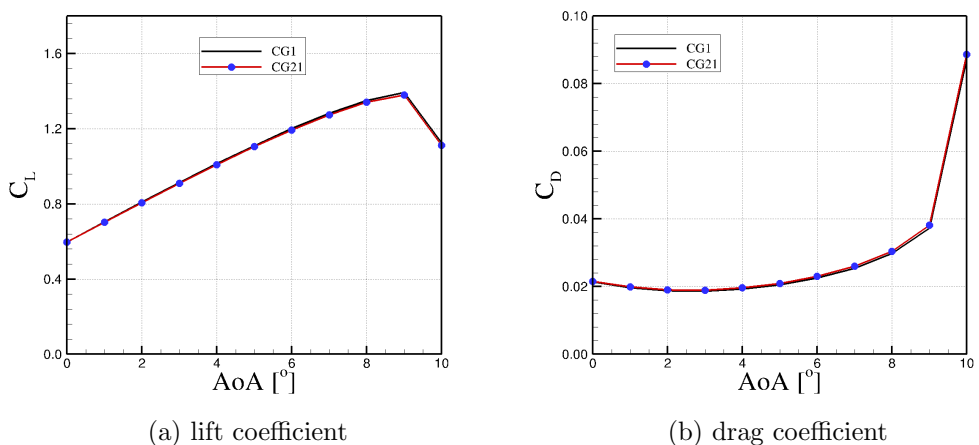
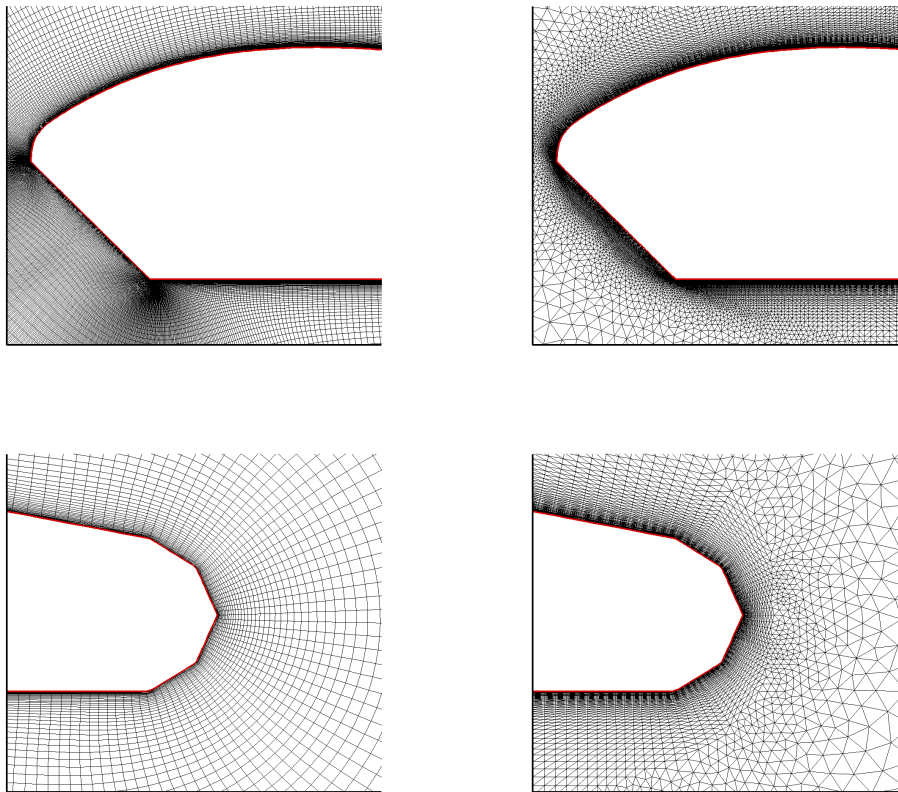


Figure 13. Lift and drag coefficients of CG1 (341,850 cells) and CG21 (133,920 cells) grids.



(a) CG21, STR, elliptic mesh

(b) CG32, UNSTR with anisotropic viscous layers

Figure 14. CG21 and CG32 grids overview.

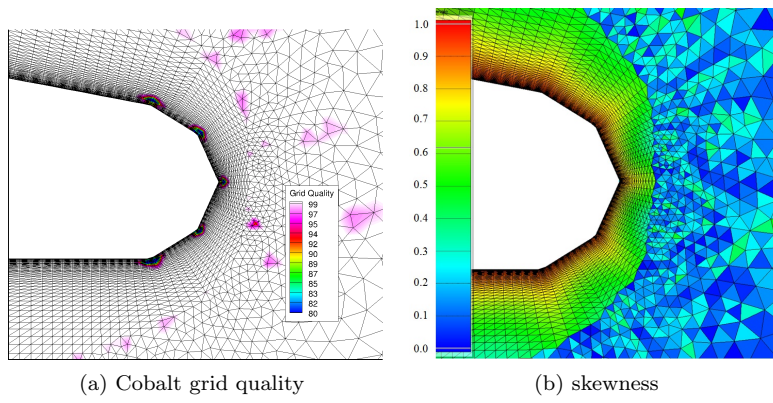


Figure 15. Cobalt cell quality versus the cell skewness report of CG32 grid.

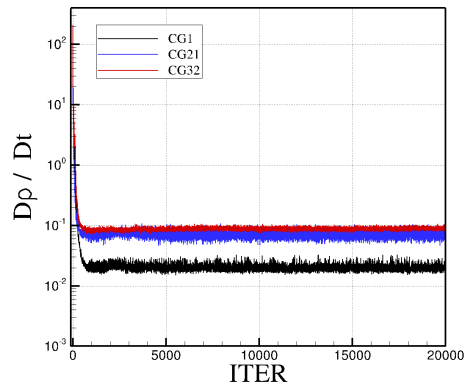


Figure 16. Density residual convergence ($D\rho/Dt$) of CG1 (STR with 341,850 cells), CG21 (STR with 133,920 cells), and CG32 (USTR with 128,564 cells).

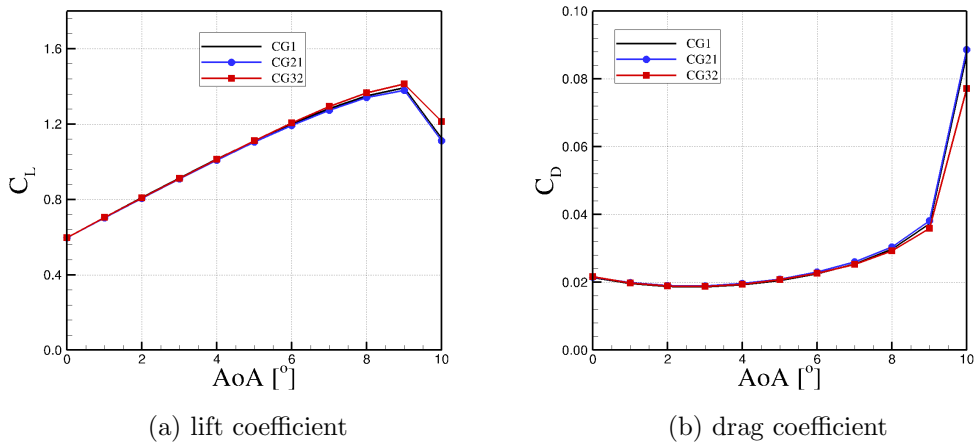


Figure 17. Lift and drag coefficients of CG1, CG21, and CG32.

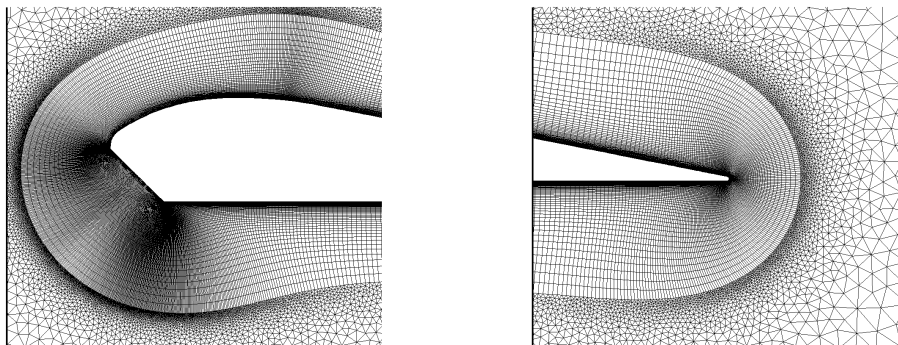


Figure 18. Hybrid mesh of CG42 with 75 prismatic layers near the wall.

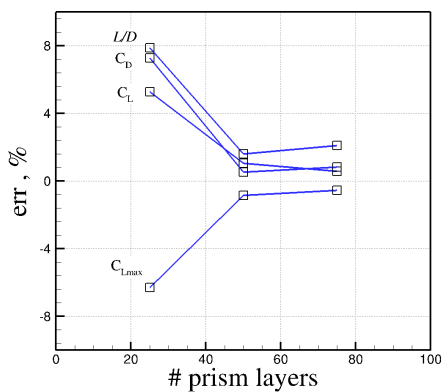


Figure 19. Solution errors against number of prism layers in the hybrid grids.

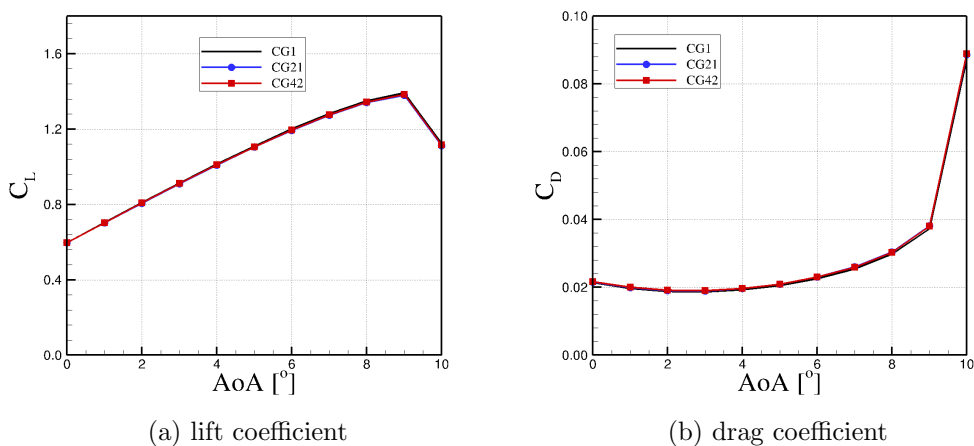


Figure 20. Lift and drag coefficients of CG42 mesh.

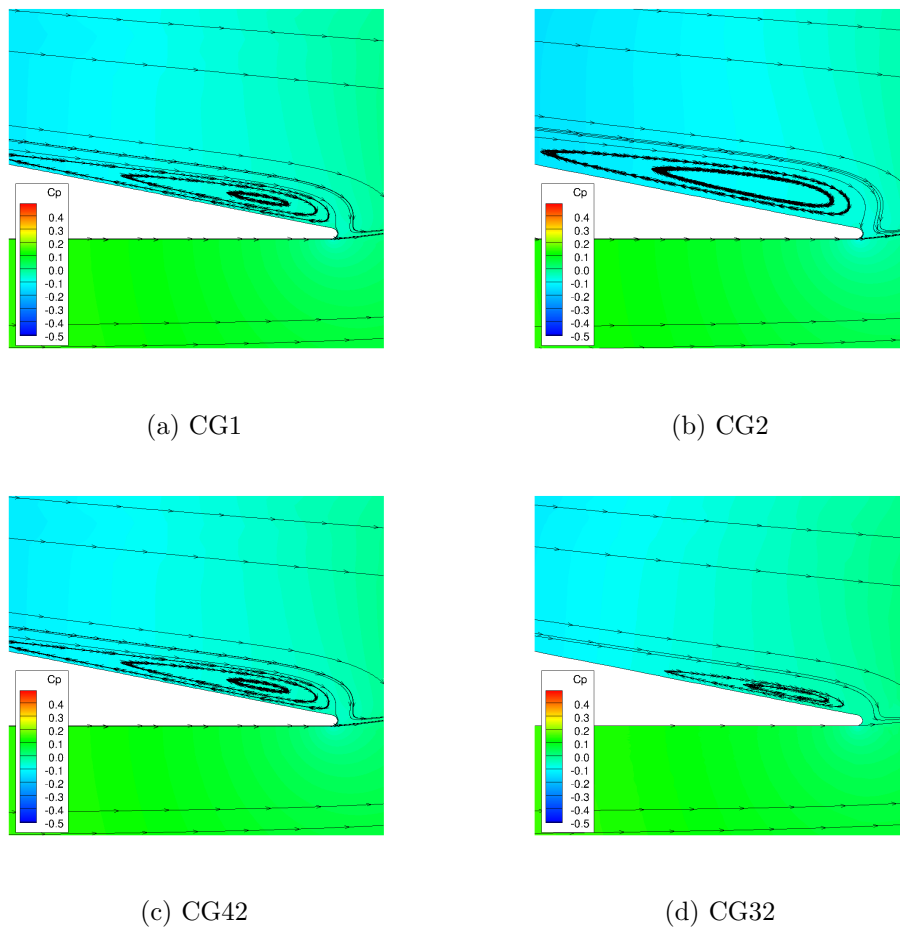


Figure 21. Flow solutions of CG1, CG2, CG32, and CG42 meshes at $\alpha = 9^\circ$.

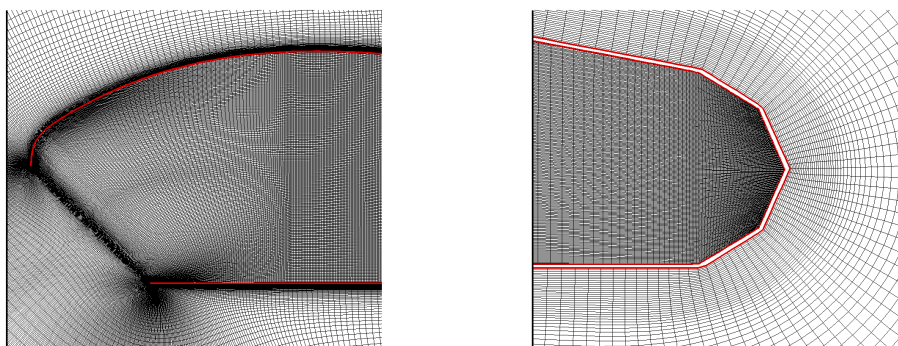


Figure 22. OG1 grid overview.

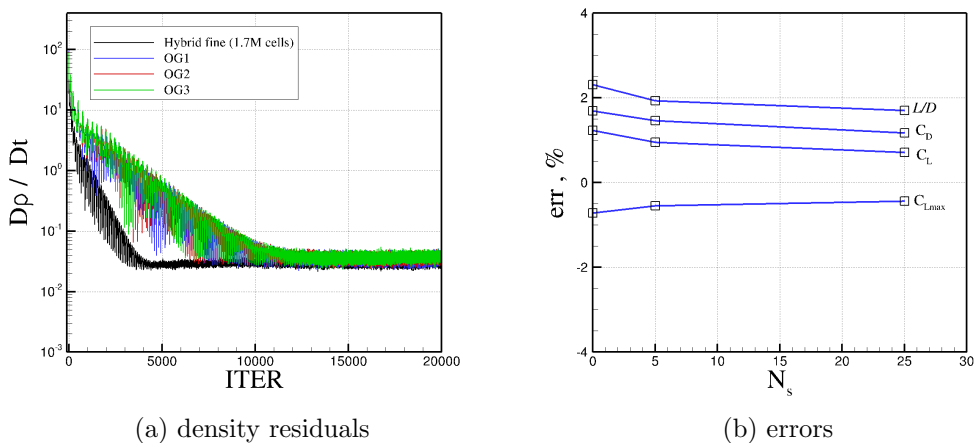


Figure 23. Effects of initial grid spacing (N_s) on the solution convergence and errors of open airfoil grids.

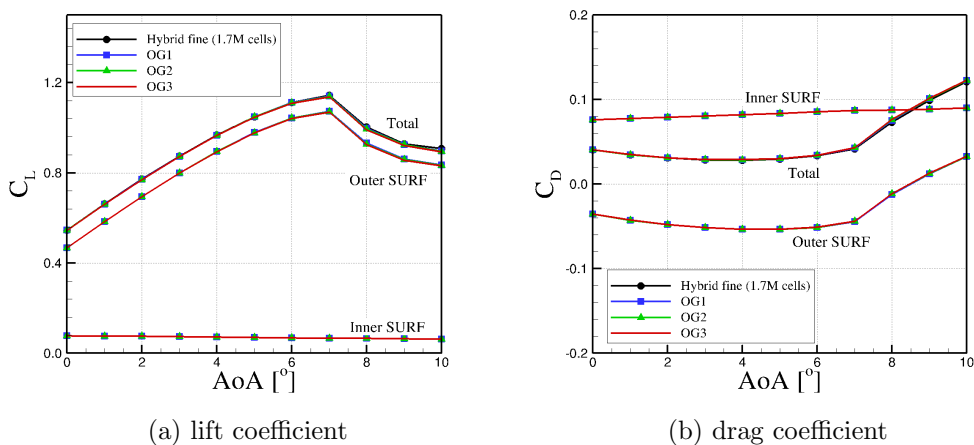


Figure 24. Lift and drag coefficients of OG1, OG2, and OG3. The coefficients were compared with the hybrid fine grid (1.7M cells) of Ref. 21.

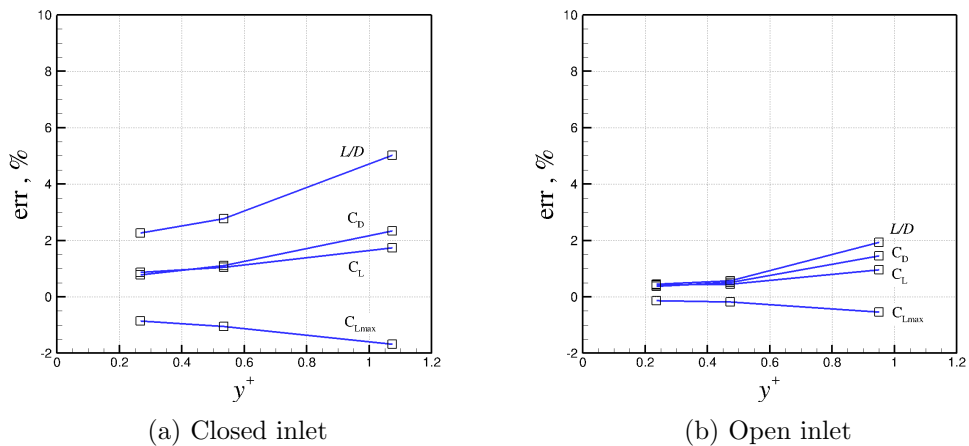


Figure 25. Effects of initial grid spacing (Δ_{s1}) on the solution errors of closed- and open-inlet grids.

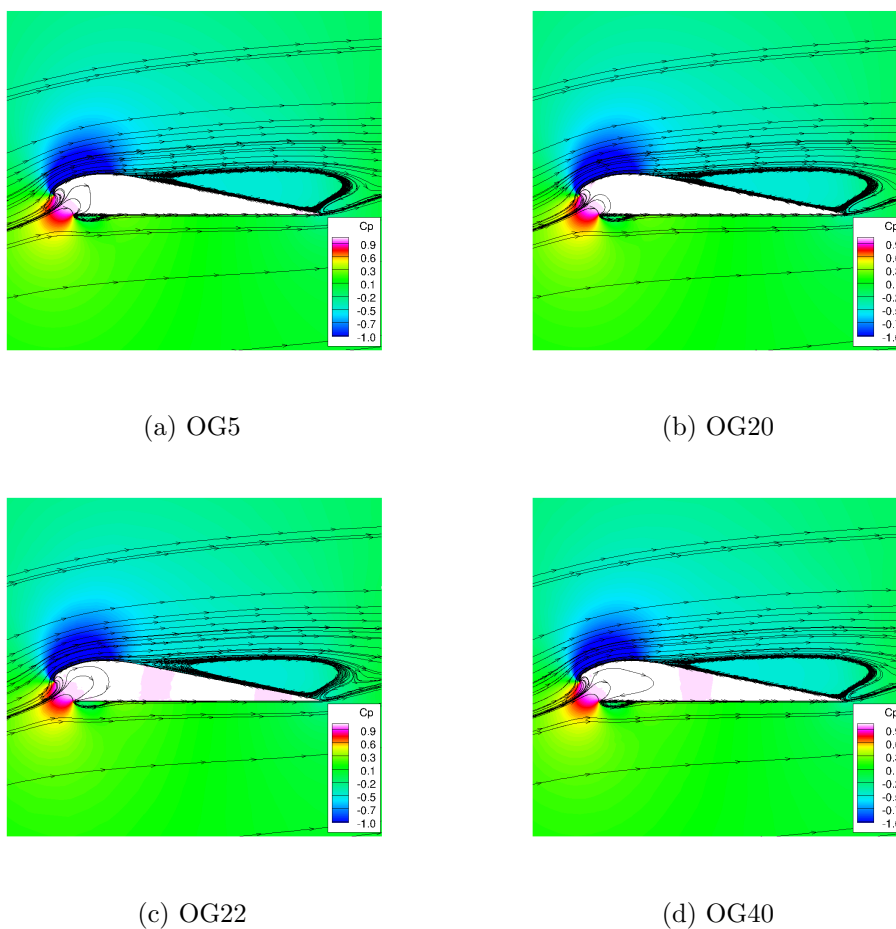
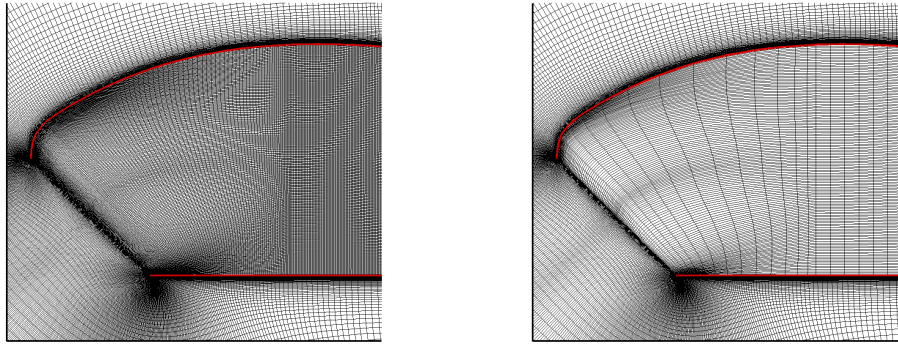


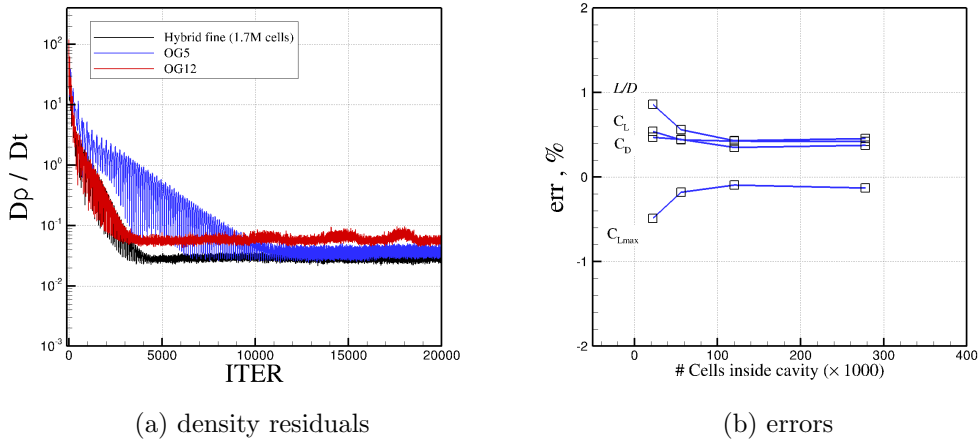
Figure 26. Flow solutions of OG5, OG20, OG22, and OG40 meshes at $\alpha = 9^\circ$.



(a) OG5

(b) OG12

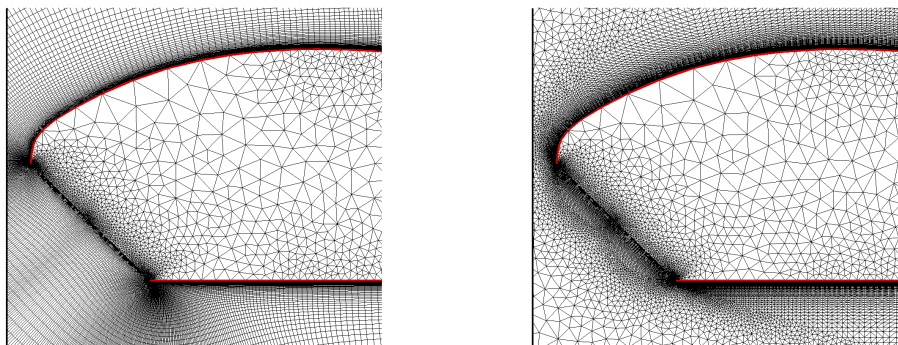
Figure 27. OG12 (with 148,262 cells) grid overview compared to OG5 mesh (with 410,260 cells).



(a) density residuals

(b) errors

Figure 28. Effects of cavity cell numbers on the solution convergence and errors of open airfoil grids.



(a) OG20

(b) OG22

Figure 29. Overview of OG20 and OG22 meshes.

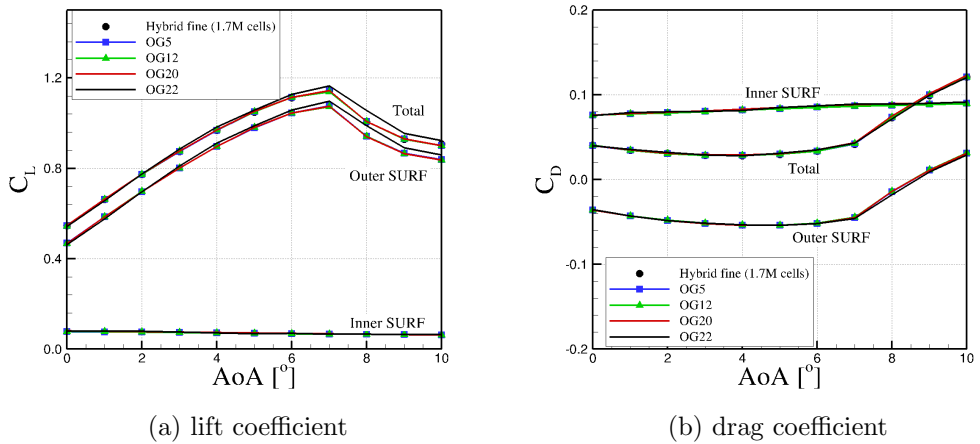


Figure 30. Lift and drag coefficients of OG5, OG12, OG20, and OG22.

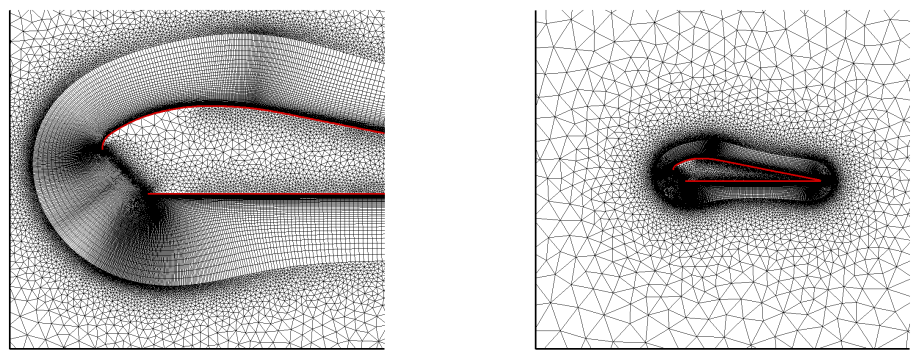


Figure 31. OG40 mesh overview.

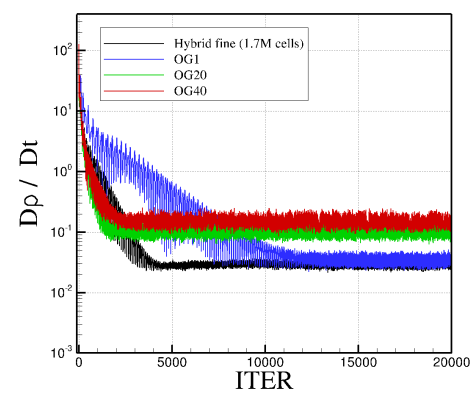
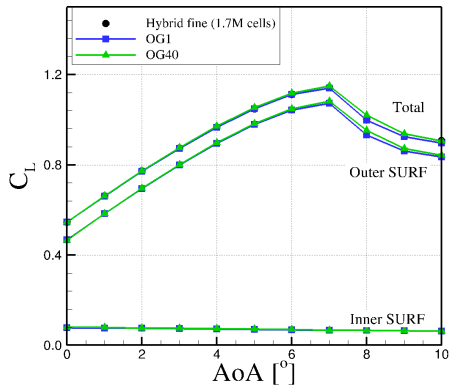
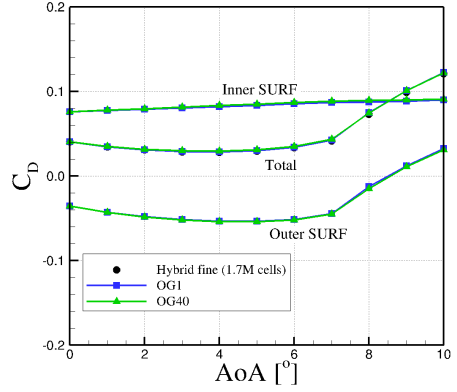


Figure 32. Density residual on the OG1, OG20, OG40 grid and the fine mesh.



(a) lift coefficient



(b) drag coefficient

Figure 33. Lift and drag coefficients predicted by the hybrid OG40 mesh.